

CP violation from charged Higgs bosons in the three Higgs doublet model

Heather E. Logan,^a Stefano Moretti,^{b,c} Diana Rojas-Ciofalo,^{c,d} and Muyuan Song^c

^a*Ottawa-Carleton Institute for Physics, Carleton University, Ottawa, Ontario K1S 5B6, Canada*

^b*Particle Physics Department, Rutherford Appleton Laboratory, Chilton, Didcot, Oxon OX11 0QX, United Kingdom*

^c*School of Physics and Astronomy, University of Southampton, Southampton, SO17 1BJ, United Kingdom*

^d*National Centre for Nuclear Research, Pasteura 7, 02-093 Warsaw, Poland*

E-mail: logan@physics.carleton.ca, S.Moretti@soton.ac.uk,
Diana.Rojas-Ciofalo@ncbj.gov.pl, ms32g13@soton.ac.uk

ABSTRACT: We demonstrate a new type of cancellation of contributions to the electron and neutron electric dipole moments (EDMs) that occurs in three Higgs doublet models (3HDMs) when CP violation appears in the charged Higgs sector. The cancellation becomes exact when the two physical charged Higgs bosons in the model are degenerate in mass. Depending on the model parameters, degeneracies at the 10% level are however sufficient to evade current bounds on the electron and neutron EDMs. We demonstrate that viable parameter space remains with both charged Higgs bosons lighter than 500 GeV and large CP-violating phases while also satisfying theoretical constraints from perturbativity and experimental ones from $\bar{B} \rightarrow X_s \gamma$ and direct searches.

Contents

1	Introduction	1
2	Three Higgs doublet model	3
2.1	Charged Higgs sector	4
2.2	The Yukawa Lagrangian	6
2.3	Collider constraints	8
2.4	Perturbativity constraints	11
3	Calculation of EDMs in the 3HDM	13
3.1	Electron EDM from charged Higgs bosons in the 3HDM	13
3.2	Neutron EDM from charged Higgs bosons in the 3HDM	15
4	Cancellation in the charged Higgs contributions to the EDMs	17
5	Numerical results	18
5.1	Light charged Higgses	19
5.1.1	The $M_{H_2^\pm} < m_t < M_{H_3^\pm}$ case	19
5.1.2	The $M_{H_2^\pm} < M_{H_3^\pm} < m_t$ case	20
5.2	Heavy charged Higgses	22
6	Conclusions	24
A	Experimental constraints from $\bar{B} \rightarrow X_s \gamma$	28
B	Charged Higgs Yukawa couplings	31

1 Introduction

In order to explain the observed baryon asymmetry of the universe [1], a new source of charge-parity (CP) violation beyond the single complex phase in the Standard Model (SM) Cabibbo-Kobayashi-Maskawa (CKM) quark mixing matrix is needed [2]. At the same time, new CP-violating physics with direct couplings to quarks or leptons is becoming increasingly tightly constrained by measurements that set stringent upper limits on the electric dipole moments (EDMs) of the neutron [3] and electron [4]. These improved limits have led particle theorists to consider models in which the additional CP violation is sequestered in a hidden or dark sector that does not couple directly to SM fermions [5–11].

However, it does remain possible to evade the EDM limits through cancellations among contributions to the EDMs while maintaining large CP-violating phases. We focus here on models with CP violation in an extended Higgs sector in which the couplings of the

additional Higgs bosons to fermions are not suppressed. Such a cancellation for the electron EDM (eEDM) was demonstrated in a CP-violating two Higgs doublet model (2HDM) in Ref. [12], in which CP-violating contributions from neutral Higgs boson couplings cancel between two different Barr-Zee diagrams.

If one considers three Higgs doublet models (3HDMs) in the presence of CP violation in the charged Higgs sector, another type of cancellation takes place in both the eEDM and neutron EDM (nEDM). Quite similarly to the Glashow-Iliopoulos-Maiani (GIM) mechanism [13] that suppresses flavor-changing neutral currents (FCNCs) induced by loop diagrams involving a sum over fermions, the cancellation in the 3HDM involves a sum over the two charged Higgs bosons of the model and becomes exact when these are degenerate in mass. However, even away from this limit and depending on the other model parameters, chiefly the charged Higgs boson Yukawa couplings, mass degeneracies of $\mathcal{O}(10\%)$ are still sufficient to evade current bounds on the electron and neutron EDMs. Under these conditions, we show that significant parameter space regions remain in a 3HDM, including regions with one or both charged Higgs bosons being lighter than m_t (the top quark mass), while simultaneously satisfying both theoretical and experimental constraints.

In this paper we focus on CP-violating effects within the charged Higgs sector of the 3HDM in which natural flavour conservation (NFC) [14, 15] ensures the absence of tree-level FCNCs via Higgs interactions. In this kind of models the Higgs sector CP violation arises from four physical CP-violating phases in the scalar potential. These phases generically lead to CP violation in both the neutral and charged Higgs sectors. Previous studies of CP violation in extended Higgs sectors have primarily focused on CP violation in the neutral scalar sector, indeed, this is the only type of Higgs sector CP violation that is possible in 2HDMs with NFC. (Removing the requirement for NFC does open the possibility of CP violation in the couplings of the single charged Higgs boson of the Aligned 2HDM, though [16].) The cancellation mechanism that we study in this paper does not appear in the Aligned 2HDM because that model contains only a single physical charged Higgs boson. To highlight the novel cancellation mechanism for CP-odd observables like the nEDM and eEDM, in this work, we will limit ourselves to the case in which CP violation appears only in the charged Higgs sector. We will show that it is possible to do this through a judicious choice of three of the four physical CP-violating phases in the scalar potential, leaving one physical phase free to control the CP violation in the charged Higgs sector. We leave a full analysis including CP violation in the neutral scalar sector of the 3HDM to future work.

This paper is organized as follows. In Sec. 2, we describe the 3HDM and define our notation. In Sec. 3, we describe the calculation of the electron and neutron EDMs. In Sec. 4, we explain the physics behind the aforementioned cancellation mechanism. In Sec. 5 we present numerical results showing the allowed CP-violating parameter space given the current EDM constraints along with constraints from $\bar{B} \rightarrow X_s \gamma$ and searches for charged Higgs bosons at colliders. In Sec. 6, we conclude. Details of our implementation of the $\bar{B} \rightarrow X_s \gamma$ and EDM constraints are given in two appendices.

Model	Φ_1	Φ_2	Φ_3
Type-I	–	u, d, ℓ	–
Type-II	d, ℓ	u	–
Type-X or Lepton-specific	ℓ	u, d	–
Type-Y or Flipped	d	u, ℓ	–
Type-Z or Democratic	d	u	ℓ

Table 1. The five types of 3HDM subject to NFC. The table indicates which Higgs doublet is responsible for generating the mass of each type of fermion, wherein $u(d)$ refers to an up(down)-type quark and ℓ to a (charged) lepton.

2 Three Higgs doublet model

The model contains three scalar $SU(2)_L$ doublets, denoted Φ_1, Φ_2, Φ_3 , with

$$\Phi_i = \begin{pmatrix} \phi_i^+ \\ (v_i + \phi_i^{0,r} + i\phi_i^{0,i})/\sqrt{2} \end{pmatrix}. \quad (2.1)$$

The vacuum expectation values (VEVs) v_i of the three Higgs doublets can be chosen real through an independent rephasing of each doublet. They are constrained by the W^\pm boson mass to satisfy $v = \sqrt{v_1^2 + v_2^2 + v_3^2} \approx 246$ GeV.

In order to avoid FCNCs through Higgs interactions, we will impose NFC [14, 15] by allowing each type of fermion to couple to only a single Higgs doublet. To this end, we require that the scalar potential be invariant under three Z_2 symmetries that each act on one of the Φ_i .¹ The transformation assignments of the fermions under the three Z_2 symmetries then dictate the Yukawa structure of the model according to the five physically-distinct “types” given in Tab. 1.

The most general $SU(2)_L \times U(1)_Y$ invariant potential subject to these Z_2 symmetries is [17]

$$\begin{aligned} V = & m_{11}^2 \Phi_1^\dagger \Phi_1 + m_{22}^2 \Phi_2^\dagger \Phi_2 + m_{33}^2 \Phi_3^\dagger \Phi_3 \\ & - [m_{12}^2 \Phi_1^\dagger \Phi_2 + m_{13}^2 \Phi_1^\dagger \Phi_3 + m_{23}^2 \Phi_2^\dagger \Phi_3 + \text{h.c.}] \\ & + \frac{1}{2} \lambda_1 (\Phi_1^\dagger \Phi_1)^2 + \frac{1}{2} \lambda_2 (\Phi_2^\dagger \Phi_2)^2 + \frac{1}{2} \lambda_3 (\Phi_3^\dagger \Phi_3)^2 \\ & + \lambda_{12} (\Phi_1^\dagger \Phi_1) (\Phi_2^\dagger \Phi_2) + \lambda_{13} (\Phi_1^\dagger \Phi_1) (\Phi_3^\dagger \Phi_3) + \lambda_{23} (\Phi_2^\dagger \Phi_2) (\Phi_3^\dagger \Phi_3) \\ & + \lambda'_{12} (\Phi_1^\dagger \Phi_2) (\Phi_2^\dagger \Phi_1) + \lambda'_{13} (\Phi_1^\dagger \Phi_3) (\Phi_3^\dagger \Phi_1) + \lambda'_{23} (\Phi_2^\dagger \Phi_3) (\Phi_3^\dagger \Phi_2) \\ & + \frac{1}{2} [\lambda''_{12} (\Phi_1^\dagger \Phi_2)^2 + \lambda''_{13} (\Phi_1^\dagger \Phi_3)^2 + \lambda''_{23} (\Phi_2^\dagger \Phi_3)^2 + \text{h.c.}], \end{aligned} \quad (2.2)$$

where we have retained the terms m_{ij}^2 that break the Z_2 symmetries softly.

The potential contains six complex parameters: the three soft-breaking masses, m_{12}^2 , m_{13}^2 , and m_{23}^2 , and three quartic couplings, λ''_{12} , λ''_{13} , and λ''_{23} . Only four of the six CP-violating phases are physical, as the other two can be eliminated by phase rotations of Φ_1 ,

¹Only two of these Z_2 symmetries need to be imposed by hand as the third follows accidentally. The Type-I version of the model can be achieved by imposing only a single Z_2 symmetry, which opens the possibility of additional terms in the scalar potential. We do not consider this possibility here, though.

Φ_2 , and Φ_3 .² Instead of removing the imaginary part of two of the six complex parameters, we use this phase freedom to make all three VEVs real and positive with no loss of generality. This choice requires that we fix the imaginary parts of m_{13}^2 and m_{23}^2 as follows [17]:

$$\text{Im}(m_{13}^2) = -\frac{v_2}{v_3}\text{Im}(m_{12}^2) + \frac{v_1 v_2^2}{2v_3}\text{Im}(\lambda''_{12}) + \frac{v_1 v_3}{2}\text{Im}(\lambda''_{13}), \quad (2.3a)$$

$$\text{Im}(m_{23}^2) = \frac{v_1}{v_3}\text{Im}(m_{12}^2) - \frac{v_1^2 v_2}{2v_3}\text{Im}(\lambda''_{12}) + \frac{v_2 v_3}{2}\text{Im}(\lambda''_{23}). \quad (2.3b)$$

The remaining four independent complex phases are responsible for the Higgs sector CP violation in the form of mixing between the two would-be CP-odd and the three would-be CP-even neutral Higgs states, as well as a complex phase in the charged Higgs mass matrix, which results in CP violation in the couplings of the charged Higgs mass eigenstates. For our purposes in this paper, we specialize to a constrained version of the model in which we turn off CP violation in the neutral scalar sector; this is achieved by imposing the following three relations:

$$\text{Im}(\lambda''_{13}) = -\frac{v_2^2}{v_3^2}\text{Im}(\lambda''_{12}), \quad (2.4a)$$

$$\text{Im}(\lambda''_{23}) = \frac{v_1^2}{v_3^2}\text{Im}(\lambda''_{12}), \quad (2.4b)$$

$$\text{Im}(m_{12}^2) = v_1 v_2 \text{Im}(\lambda''_{12}). \quad (2.4c)$$

This leaves only one independent CP-violating parameter, which can be taken as $\text{Im}(\lambda''_{12})$. The remaining CP-violating phase appears in the charged Higgs mass matrix.

Finally, minimizing the potential also allows three real parameters to be eliminated in favor of the (real) VEVs [17]:

$$m_{11}^2 = \frac{v_2}{v_1}\text{Re}(m_{12}^2) + \frac{v_3}{v_1}\text{Re}(m_{13}^2) - \frac{v_1^2}{2}\lambda_1 - \frac{v_2^2}{2}[\lambda_{12} + \lambda'_{12} + \text{Re}(\lambda''_{12})] - \frac{v_3^2}{2}[\lambda_{13} + \lambda'_{13} + \text{Re}(\lambda''_{13})], \quad (2.5a)$$

$$m_{22}^2 = \frac{v_1}{v_2}\text{Re}(m_{12}^2) + \frac{v_3}{v_2}\text{Re}(m_{23}^2) - \frac{v_2^2}{2}\lambda_2 - \frac{v_1^2}{2}[\lambda_{12} + \lambda'_{12} + \text{Re}(\lambda''_{12})] - \frac{v_3^2}{2}[\lambda_{23} + \lambda'_{23} + \text{Re}(\lambda''_{23})], \quad (2.5b)$$

$$m_{33}^2 = \frac{v_1}{v_3}\text{Re}(m_{13}^2) + \frac{v_2}{v_3}\text{Re}(m_{23}^2) - \frac{v_3^2}{2}\lambda_3 - \frac{v_1^2}{2}[\lambda_{13} + \lambda'_{13} + \text{Re}(\lambda''_{13})] - \frac{v_2^2}{2}[\lambda_{23} + \lambda'_{23} + \text{Re}(\lambda''_{23})]. \quad (2.5c)$$

2.1 Charged Higgs sector

CP violation in the charged Higgs sector emerges from the mixing of the gauge eigenstates ϕ_i^+ ($i = 1, 2, 3$) to form the charged Higgs mass eigenstates. Following the notation of

²Only relative phase rotations are physically meaningful. A common overall phase rotation of all three doublets corresponds to the $U(1)_Y$ hypercharge symmetry and has no effect on the potential. This overall phase rotation can be used to choose one of the VEVs to be real and positive; we apply this to v_3 .

Ref. [17], we define a mixing matrix U according to

$$\begin{pmatrix} \phi_1^+ \\ \phi_2^+ \\ \phi_3^+ \end{pmatrix} = U^\dagger \begin{pmatrix} G^+ \\ H_2^+ \\ H_3^+ \end{pmatrix}, \quad (2.6)$$

where G^+ is the charged Goldstone boson, and H_2^+ and H_3^+ are the physical charged Higgs mass eigenstates. Here, U is obtained by diagonalizing the charged Higgs mass-squared matrix, $V \supset \phi_i^- (\mathcal{M}_{H^\pm}^2)_{ij} \phi_j^+$, where [17]

$$\mathcal{M}_{H^\pm}^2 = \begin{pmatrix} \frac{v_2}{v_1} A_{12} + \frac{v_3}{v_1} A_{13} & -A_{12} + iB & -A_{13} - i\frac{v_2}{v_3} B \\ -A_{12} - iB & \frac{v_1}{v_2} A_{12} + \frac{v_3}{v_2} A_{23} & -A_{23} + i\frac{v_1}{v_3} B \\ -A_{13} + i\frac{v_2}{v_3} B & -A_{23} - i\frac{v_1}{v_3} B & \frac{v_1}{v_3} A_{13} + \frac{v_2}{v_3} A_{23} \end{pmatrix}, \quad (2.7)$$

with

$$\begin{aligned} A_{12} &= \text{Re}(m_{12}^2) - \frac{v_1 v_2}{2} [\lambda'_{12} + \text{Re}(\lambda''_{12})], \\ A_{23} &= \text{Re}(m_{23}^2) - \frac{v_2 v_3}{2} [\lambda'_{23} + \text{Re}(\lambda''_{23})], \\ A_{13} &= \text{Re}(m_{13}^2) - \frac{v_1 v_3}{2} [\lambda'_{13} + \text{Re}(\lambda''_{13})], \\ B &= -\text{Im}(m_{12}^2) + \frac{v_1 v_2}{2} \text{Im}(\lambda''_{12}). \end{aligned} \quad (2.8)$$

Notice that CP violation enters only via B . In the case that we turn off CP violation in the neutral Higgs sector by imposing Eqs. (2.4), B becomes

$$B = -\frac{v_1 v_2}{2} \text{Im}(\lambda''_{12}).$$

We now diagonalize the charged Higgs mass matrix. We perform the rotation in two stages, starting with rotating to the Higgs basis using the rotation matrix

$$U_1 = \begin{pmatrix} \sin \gamma & 0 & \cos \gamma \\ 0 & 1 & 0 \\ -\cos \gamma & 0 & \sin \gamma \end{pmatrix} \begin{pmatrix} \cos \beta & \sin \beta & 0 \\ -\sin \beta & \cos \beta & 0 \\ 0 & 0 & 1 \end{pmatrix}, \quad (2.9)$$

where we define the angles β and γ in terms of the VEVs:

$$\tan \beta = \frac{v_2}{v_1}, \quad \tan \gamma = \frac{\sqrt{v_1^2 + v_2^2}}{v_3}. \quad (2.10)$$

This rotation isolates the charged Goldstone boson, yielding the following mass matrix:

$$\mathcal{M}_{H^\pm}^2 = U_1 \mathcal{M}_{H^\pm}^2 U_1^\dagger = \begin{pmatrix} 0 & 0 & 0 \\ 0 & \mathcal{M}_{22}^{\prime 2} & \mathcal{M}_{23}^{\prime 2} \\ 0 & \mathcal{M}_{23}^{\prime 2*} & \mathcal{M}_{33}^{\prime 2} \end{pmatrix}, \quad (2.11)$$

where [17]:³

$$\mathcal{M}_{22}^{\prime 2} = \frac{v_{12}^2}{v_1 v_2} A_{12} + \frac{v_2^2 v_3}{v_1 v_{12}^2} A_{13} + \frac{v_1^2 v_3}{v_2 v_{12}^2} A_{23}, \quad (2.12)$$

$$\mathcal{M}_{33}^{\prime 2} = \frac{v_1 v^2}{v_3 v_{12}^2} A_{13} + \frac{v_2 v^2}{v_3 v_{12}^2} A_{23}, \quad (2.13)$$

$$\mathcal{M}_{23}^{\prime 2} = \frac{v_2 v}{v_{12}^2} A_{13} - \frac{v_1 v}{v_{12}^2} A_{23} + i \frac{v}{v_3} B, \quad (2.14)$$

and $v_{12}^2 = v_1^2 + v_2^2$. The next step is to diagonalize the matrix in Eq. (2.11). We do it with the matrix U_2 ,

$$U_2 = \begin{pmatrix} 1 & 0 & 0 \\ 0 & e^{-i\delta} & 0 \\ 0 & 0 & 1 \end{pmatrix} \begin{pmatrix} 1 & 0 & 0 \\ 0 & \cos \theta & \sin \theta e^{i\delta} \\ 0 & -\sin \theta e^{-i\delta} & \cos \theta \end{pmatrix}, \quad (2.15)$$

where the CP-violating phase δ is given by

$$\delta = \text{phase}(\mathcal{M}_{23}^{\prime 2}), \quad (2.16)$$

with $0 \leq \delta < 2\pi$. For later convenience, we choose the mixing angle θ to lie in the range $-\pi/2 \leq \theta \leq 0$,⁴ so that either H_2^\pm or H_3^\pm can be the lighter physical charged Higgs boson.

The full rotation matrix in Eq. (2.6) is then given explicitly by [17]:

$$U^\dagger = (U_2 U_1)^\dagger = \begin{pmatrix} s_\gamma c_\beta - c_\theta s_\beta e^{i\delta} - s_\theta c_\gamma c_\beta & s_\theta s_\beta e^{i\delta} - c_\theta c_\gamma c_\beta \\ s_\gamma s_\beta & c_\theta c_\beta e^{i\delta} - s_\theta c_\gamma s_\beta & -s_\theta c_\beta e^{i\delta} - c_\theta c_\gamma s_\beta \\ c_\gamma & s_\theta s_\gamma & c_\theta s_\gamma \end{pmatrix}, \quad (2.17)$$

where $s_\beta = \sin \beta$, $c_\beta = \cos \beta$ and similarly for the other mixing angles. We give the explicit form for U^\dagger rather than U for later convenience in writing the Yukawa couplings.

For simplicity, we assume that the masses of all the extra neutral scalars, that is, $H_{2,3}$ and $A_{2,3}$, are larger than those of the charged Higgs bosons, and we take the alignment limit so that the tree-level couplings of the 125 GeV Higgs boson h are identical to those of the SM Higgs boson. In other words, we focus on the physics related to the charged Higgs sector so that our input parameters are the following six:

$$M_{H_2^\pm}, M_{H_3^\pm}, \tan \beta, \tan \gamma, \theta, \delta.$$

Notice that our definitions of $\tan \beta$ and $\tan \gamma$ differ from those in Ref. [18], where a similar analysis of the 3HDM was performed.

2.2 The Yukawa Lagrangian

In what follows, we will focus on the Democratic 3HDM,⁵ in which Φ_1 gives mass to down-type quarks, Φ_2 gives mass to up-type quarks, and Φ_3 gives mass to charged leptons. This

³We correct two typos in the expression for $\mathcal{M}_{22}^{\prime 2}$ in Eq. (A8) of Ref. [17].

⁴In the Democratic (or Type-Z) 3HDM, the coupling of H_2^+ to leptons goes to zero when $\theta = 0$, likewise the coupling of H_3^+ to leptons goes to zero when $\theta = -\pi/2$.

⁵Hereafter, we adopt this nomenclature in preference to Type-Z, as the former was introduced in Ref. [17] prior to the latter in Ref. [18].

Model	X_i	Y_i	Z_i
Type-I	$\frac{U_{2i}^\dagger}{U_{21}^\dagger}$	$-\frac{U_{2i}^\dagger}{U_{21}^\dagger}$	$\frac{U_{2i}^\dagger}{U_{21}^\dagger}$
Type-II	$\frac{U_{1i}^\dagger}{U_{11}^\dagger}$	$-\frac{U_{2i}^\dagger}{U_{21}^\dagger}$	$\frac{U_{1i}^\dagger}{U_{11}^\dagger}$
Type-X or Lepton-specific	$\frac{U_{2i}^\dagger}{U_{21}^\dagger}$	$-\frac{U_{2i}^\dagger}{U_{21}^\dagger}$	$\frac{U_{1i}^\dagger}{U_{11}^\dagger}$
Type-Y or Flipped	$\frac{U_{1i}^\dagger}{U_{11}^\dagger}$	$-\frac{U_{2i}^\dagger}{U_{21}^\dagger}$	$\frac{U_{2i}^\dagger}{U_{21}^\dagger}$
Type-Z or Democratic	$\frac{U_{1i}^\dagger}{U_{11}^\dagger}$	$-\frac{U_{2i}^\dagger}{U_{21}^\dagger}$	$\frac{U_{3i}^\dagger}{U_{31}^\dagger}$

Table 2. Coefficients X_i , Y_i , and Z_i appearing in the Yukawa Lagrangian for the H_i^+ couplings to down-type quarks, up-type quarks, and (charged) leptons, respectively, with $i = 2, 3$. The matrix U^\dagger is defined in Eq. (2.17).

version of the model gives rise to the most interesting EDM phenomenology arising from CP violation in the charged Higgs mixing matrix. We will comment on the EDMs in the other versions of the 3HDM in Sec. 4.

The Yukawa Lagrangian takes the form

$$\mathcal{L}_{\text{Yukawa}} = -\{\bar{Q}_L \Phi_1 \mathcal{G}_d d_R + \bar{Q}_L \tilde{\Phi}_2 \mathcal{G}_u u_R + \bar{L}_L \Phi_3 \mathcal{G}_l l_R + \text{h.c.}\}, \quad (2.18)$$

where $\tilde{\Phi}$ is the conjugate doublet given by $i\sigma^2 \Phi^*$. Here, \mathcal{G}_f are the Yukawa matrices, which are determined in terms of the fermion mass matrices \mathcal{M}_f by $\mathcal{M}_f = \mathcal{G}_f v_i / \sqrt{2}$.

The Yukawa couplings of the charged Higgs bosons are given by [19]:

$$\begin{aligned} \mathcal{L}_{\text{Yukawa}}^{\text{charged}} = & -\frac{\sqrt{2}}{v} \{ [X_2 \bar{u}_L V \mathcal{M}_d d_R + Y_2 \bar{u}_R \mathcal{M}_u V d_L + Z_2 \bar{\nu}_L \mathcal{M}_l l_R] H_2^+ \\ & + [X_3 \bar{u}_L V \mathcal{M}_d d_R + Y_3 \bar{u}_R \mathcal{M}_u V d_L + Z_3 \bar{\nu}_L \mathcal{M}_l l_R] H_3^+ + \text{h.c.} \}, \end{aligned} \quad (2.19)$$

where V is the CKM matrix and the coupling coefficients X_i , Y_i and Z_i are given in terms of the elements of the charged Higgs mixing matrix U^\dagger in Eq. (2.17) by

$$X_i = \frac{U_{1i}^\dagger}{U_{11}^\dagger}, \quad Y_i = -\frac{U_{2i}^\dagger}{U_{21}^\dagger}, \quad Z_i = \frac{U_{3i}^\dagger}{U_{31}^\dagger}, \quad (2.20)$$

where $i = 2, 3$. Note that these expressions are for the Democratic 3HDM. The coupling coefficients for the other types of 3HDM are collected in Tab. 2.⁶

In Figs. 1–2, we show the branching ratios (BRs) of H_2^\pm (upper panels) and H_3^\pm (lower panels) as a function of $\tan \beta$, in the 3HDM Type-II, -X, -Y and the Democratic model.⁷ In Fig. 1 we take $M_{H_2^\pm} = 100$ GeV and $M_{H_3^\pm} = 150$ GeV, while in Fig. 2 we take $M_{H_2^\pm} = 200$ GeV and $M_{H_3^\pm} = 250$ GeV, with $\theta = -\pi/4$ and $\delta = 0$ in both. The solid and dotted curves show the case for $\tan \beta = 2$ and 5, respectively. We can see that a light charged

⁶In all types of 3HDM except the Democratic one, taking the limit $\tan \gamma \rightarrow \infty$ (i.e., $v_3 \rightarrow 0$) recovers the corresponding 2HDM plus a third, inert, doublet.

⁷We have used CalcHEP [20] to produce these plots. We will use it again to calculate widths and cross sections to compare against experimental constraints.

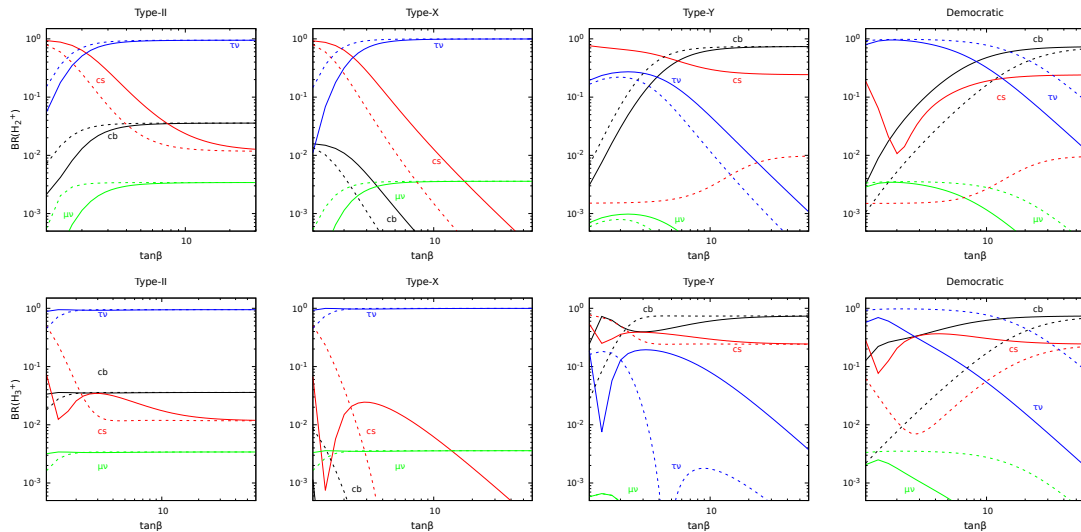


Figure 1. BRs of H_2^+ (upper panels) and H_3^+ (lower panels) as a function of $\tan\beta$ in, from left to right, the Type-II, -X, -Y, and Democratic 3HDMs. We take $M_{H_2^+} = 100$ GeV, $M_{H_3^+} = 150$ GeV, $\theta = -\pi/4$ and $\delta = 0$. The value of $\tan\gamma$ is 2 (5) for the solid (dotted) curves.

Higgs boson (with $M_{H_i^\pm} < m_t$) predominantly decays to $\tau\nu$, although cs is more dominant for some types in specific $\tan\beta$ regions. Furthermore, the decay into cb becomes relevant for higher $\tan\beta$ in the Type-Y and Democratic models. For a heavy charged Higgs boson (with $M_{H_i^\pm} > m_t$), the vastly dominant decay is into tb except for Type-X at large $\tan\beta$, where $\tau\nu$ dominates instead. Instead, for the Democratic model, $\tau\nu$ dominates for large values of $\tan\gamma$. (Notice that, here, the 3HDM parameter values are chosen so we can directly compare with Figs. 1 and 2 of [18], where the parametrization of $\tan\beta$ and $\tan\gamma$ is, however, chosen differently from our work.⁸) We do not show the BRs for the charged Higgs bosons in the Type-I 3HDM because they are independent of $\tan\beta$, are the same for both of the charged Higgs bosons, and depend very little on the charged Higgs boson mass for $M_{H_i^\pm} < m_t$. The most important BRs for the masses shown are to cs (close to 70%) and $\tau\nu$ (a little less than 30%), with sub-dominant decays to cb (just over 1%) and $\mu\nu$ (around 0.1%). When the charged Higgs masses are above the top one - in the Type-I 3HDM, decays to tb become overwhelmingly dominant, e.g., for the parameter choices of Fig. 2, all of the decay BRs to fermion pairs other than tb are below 0.2%.

2.3 Collider constraints

Charged Higgs boson production in hadronic collisions can be described by the subprocesses $gg, q\bar{q} \rightarrow t\bar{b}H^- + \text{c.c.}$ for both light ($M_{H_i^\pm} < m_t$) and heavy ($M_{H_i^\pm} > m_t$) states [21, 22], as in the former case the dominant channel is $gg, q\bar{q} \rightarrow t\bar{t} \rightarrow t\bar{b}H^- + \text{c.c.}$ (i.e., t -quark pair production and decay) while in the latter case, it is $bg \rightarrow tH^- + \text{c.c.}$ (i.e., Higgs-strahlung off b -quarks).⁹ Since the Higgs-strahlung cross section is much smaller than the one for top-

⁸Furthermore, we use here the labeling $H_{2,3}^\pm$ in place of $H_{1,2}^\pm$ in Ref. [18], respectively.

⁹Recall that b -(anti)quarks are produced inside protons from a gluon splitting.

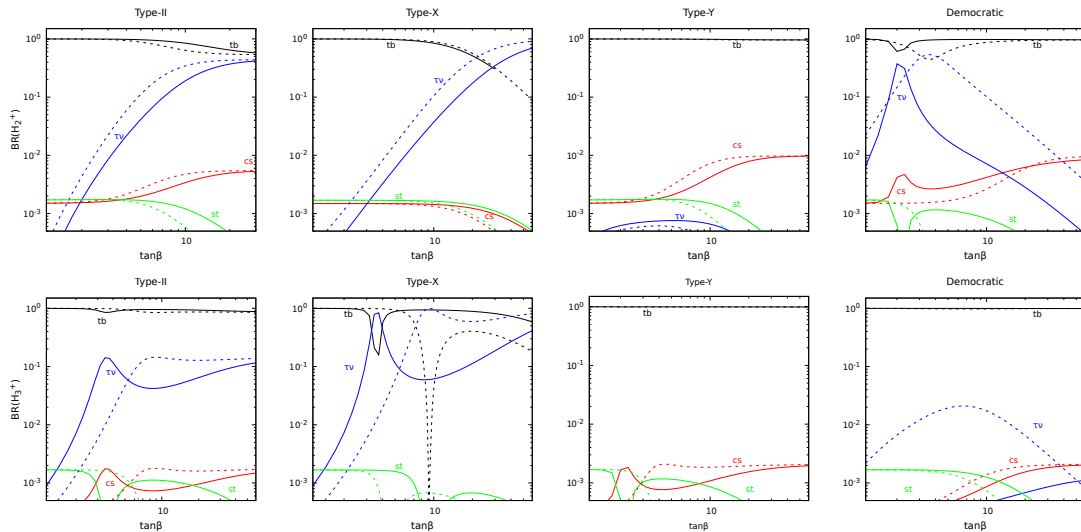


Figure 2. As in Fig. 1 but for $M_{H_2^\pm} = 200$ GeV and $M_{H_3^\pm} = 250$ GeV.

antitop quark production, a light charged Higgs boson is severely constrained while direct searches for a heavy one leave it largely unconstrained. However, when $M_{H_i^\pm} \approx M_{W^\pm} \approx 80$ GeV, the $t \rightarrow bW^+$ background overwhelms the $t \rightarrow bH^+$ signal, so that, even at the current Large Hadron Collider (LHC), this mass region is still allowed for a charged Higgs state in a 3HDM, no matter its decay mode [23, 24]. Of relevance to our analysis are the constraints coming from $H^\pm \rightarrow \tau\nu$ [25], cb [26] and cs [27] searches at the LHC (with the first channel generally being more constraining than the second and third ones), which have been performed by both ATLAS and CMS.

In Fig. 3, we fix the values of $M_{H_2^\pm} = 80$ GeV, $M_{H_3^\pm} = 170$ (200) GeV in the upper (lower) panels and $\tan\beta = 20$.¹⁰ We tested the region $-0.6 < \theta < 0$, $0.4 < \tan\gamma < 2.6$ against CMS searches for $H^\pm \rightarrow \tau\nu$ [25].¹¹ In the case of H_2^\pm , it is preferable to take values of θ closer to zero, which is in tension with the cross section for H_3^\pm , which prefers $\theta \lesssim -0.4$. However, we can quench this tension if we choose $\tan\gamma \lesssim 2$, as the BR of both charged Higgs states to $\tau\nu$ are smaller (see Fig. 1). We can also notice that lower values for $M_{H_3^\pm}$ increase the cross section of $H_3^\pm \rightarrow \tau\nu$, thus making it harder to agree with collider limits. For example, this is very manifest for the case of $M_{H_3^\pm} = 150$ GeV, shown in Fig. 4, a scenario that is excluded by $H_3^\pm \rightarrow \tau\nu$ results. For this value of $M_{H_3^\pm}$, we should also compare to the collider limits for $H_3^\pm \rightarrow cb$ and cs . However, these are less constraining than the case of $\tau\nu$. In the case when $m_t < M_{H_2^\pm} < M_{H_3^\pm}$, the BR of H_2^\pm to $\tau\nu$ only dominates over the BR to tb for small values of $\tan\beta$, as can be seen in Fig. 2. Later in this work, when we consider the masses of the charged Higgs bosons to be larger than the top-quark one, we take $\tan\beta > 10$, and then this region readily satisfies collider

¹⁰Comparing the upper and lower left panels of Fig. 3 shows that the cross section times BR of H_2^\pm is essentially unaffected by the mass of the heavier H_3^\pm , once it is at least comparable to the top quark mass.

¹¹Although values of $\tan\gamma > 2.6$ are allowed, we have chosen this region to better show the tension between the excluded areas for H_2^\pm and H_3^\pm , respectively.

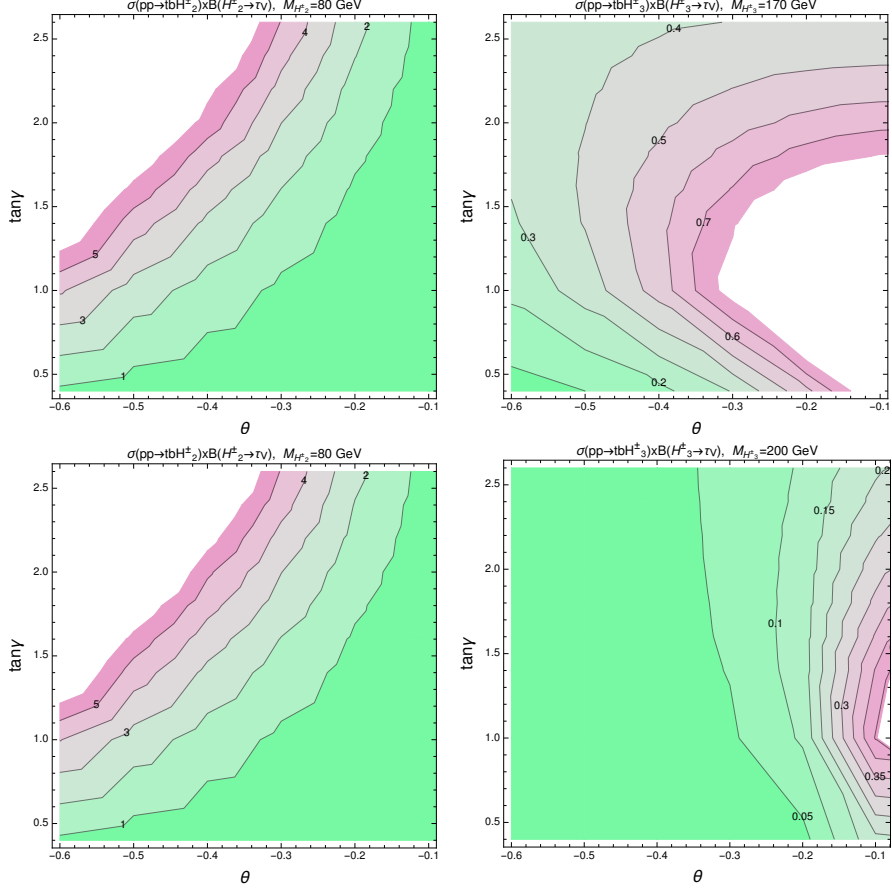


Figure 3. Contour plots of $\sigma(pp \rightarrow tbH_i^\pm) \times \text{BR}(H_i^\pm \rightarrow \tau\nu)$ for H_2^\pm (left panels) and H_3^\pm (right panels) on the $(\theta, \tan\gamma)$ plane, for $\tan\beta = 20$, $\delta = 0.9\pi$, $M_{H_2^\pm} = 80$ GeV, and $M_{H_3^\pm} = 170$ GeV (upper) and 200 GeV (lower). In the case of H_2^\pm (H_3^\pm), the resulting rate is higher for lower (higher) values of θ . The area in white is excluded by CMS [25]. The lower the mass of H_3^\pm , the more challenging it is to find viable parameter space satisfying the direct experimental search bounds for both charged scalars.

limits. Overall, notice that there is no significant interference between H_2^\pm and H_3^\pm , unless their mass difference is comparable to either of their widths, which is never the case for the benchmark points that we will study.¹²

Charged Higgs boson parameters can also be constrained indirectly via measurements of the top-quark width, Γ_t , whenever $M_{H_i^\pm} < m_t$. We add to the SM top quark width [28] the partial width from the decays $t \rightarrow H_i^\pm b$, where [23]

$$\Gamma(t \rightarrow H_i^\pm b) = \frac{G_F m_t}{8\sqrt{2}\pi} [m_t^2 |Y_i|^2 + m_b^2 |X_i|^2] \left(1 - M_{H_i^\pm}^2/m_t^2\right)^2, \quad (2.21)$$

¹²When both charged Higgs boson masses are lower than m_t , their widths become very small, so that very strong fine-tuning of their masses would be needed to achieve overlap of the lineshapes and thus interference in top quark decays involving on-shell H_2^\pm and H_3^\pm . For example, if we take the parameter values of Fig. 16 (lower panels), the width of H_2^\pm is around 5 MeV and the width of H_3^\pm is 0.9 MeV (0.74 MeV) for $\delta = 0.8\pi$ (0.95 π).

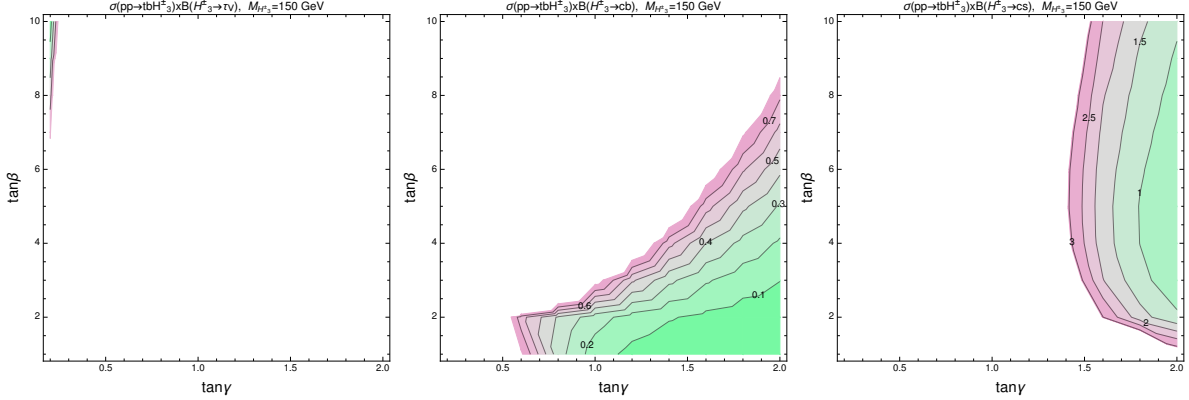


Figure 4. Production cross sections times BR for a 150 GeV heavier charged Higgs H_3^\pm decaying to $\tau\nu$ (left), cb (middle) and cs (right) in the $(\tan\gamma, \tan\beta)$ plane, for $M_{H_2^\pm} = 80$ GeV, $\theta = -0.5$, and $\delta = 0.95\pi$. The white area represents the upper limits from LHC searches in Refs. [25] (CMS), [26] (CMS), and [27] (ATLAS), respectively. Notice that the $H_3^\pm \rightarrow \tau\nu$ limits strongly exclude almost all of this scenario. The H_2^\pm signal on the other hand is well below the collider limits.

with X_i, Y_i given in Eq. (2.20). This can be done by measuring Γ_t from the top-quark visible decay products reconstructing its Breit-Wigner (BW) resonance.¹³ According to Refs. [28, 29], the most precise measurement to date is $\Gamma_t = (1.9 \pm 0.5)$ GeV. As can be seen from Fig. 5, to prevent the top-quark width from becoming too large, we need to select lower values of $\tan\beta$. Low values of $\tan\gamma$, in general, make the value of Γ_t blow up. However, in a scenario where the masses of the two charged Higgs bosons are close to the top-quark mass, we can still find very low values of $\tan\gamma$ that give an allowed Γ_t value. This will be relevant to find parameter space that can satisfy all constraints: from the top-quark width to collider searches for H_i^\pm states, EDMs, and $\bar{B} \rightarrow X_s\gamma$.

2.4 Perturbativity constraints

The ranges of $\tan\beta$ and $\tan\gamma$ can be constrained by requiring that the Yukawa couplings in Eq. (2.18) remain sufficiently perturbative. We adopt the approach introduced for the 2HDM in Ref. [30], which required the decay width Γ_{H^+} of the charged Higgs boson into $t\bar{b}$ computed above the kinematic threshold to be no larger than $M_{H^+}/2$. For example, at low $\tan\beta$, this leads to a constraint in the 2HDM Type-I of the form [30]

$$\Gamma(H^+ \rightarrow t\bar{b}) \simeq \frac{3G_F m_t^2}{4\sqrt{2}\pi \tan^2\beta} M_{H^+} < \frac{1}{2} M_{H^+}, \quad \text{or} \quad \tan\beta \gtrsim 0.34, \quad (2.22)$$

where we have used $m_t = 173$ GeV. In the 2HDM Type-II, we can use the same approach to find an upper bound on $\tan\beta$, where at large $\tan\beta$ the bottom quark Yukawa dominates, and we have

$$\Gamma(H^+ \rightarrow t\bar{b}) \simeq \frac{3G_F m_b^2 \tan^2\beta}{4\sqrt{2}\pi} M_{H^+} < \frac{1}{2} M_{H^+}, \quad \text{or} \quad \tan\beta \lesssim 125, \quad (2.23)$$

¹³Notice that, for our analysis, constraints obtained from measuring the single-top cross section are inapplicable, as these assume that $t \rightarrow bW^+$ is the only possible top-quark decay channel.

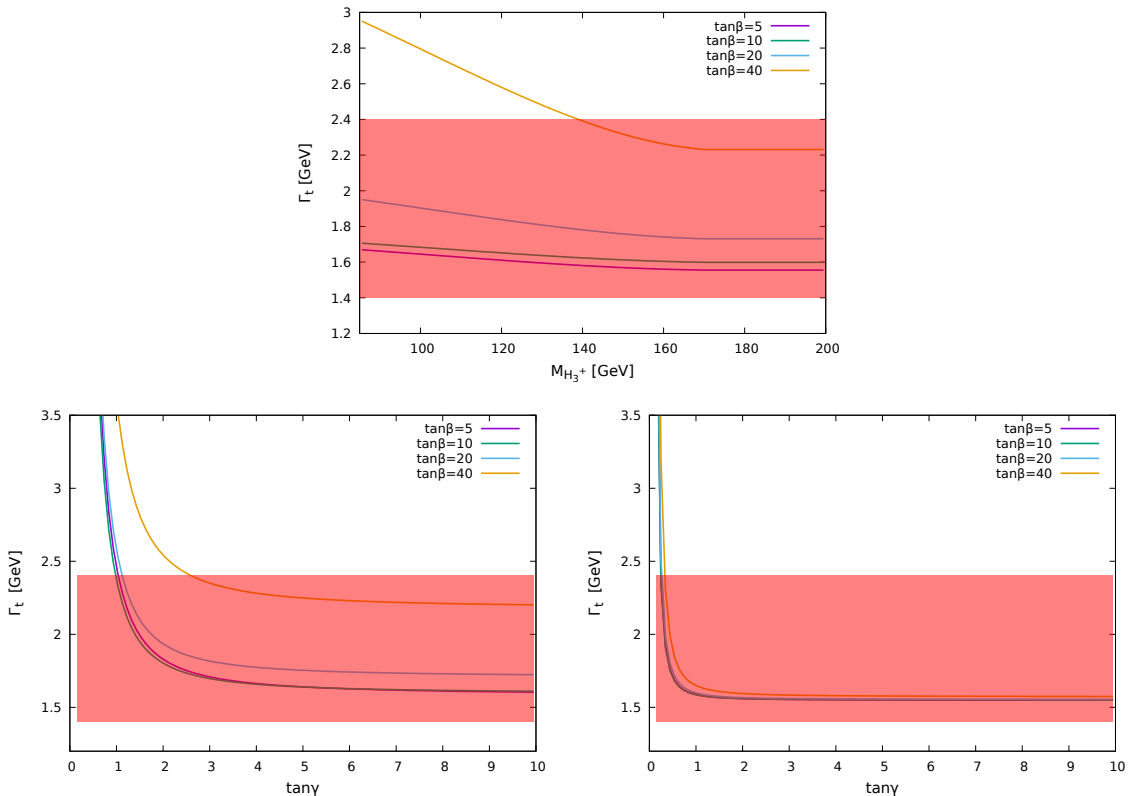


Figure 5. Predicted top quark width Γ_t as a function of $M_{H_3^+}$ (upper) and $\tan \gamma$ (lower) in the Democratic 3HDM, for $\theta = -\pi/4$ and various values of $\tan \beta$. In the upper panel $M_{H_2^+} = 85$ GeV, $\tan \gamma = 4$, and $\delta = 0.85\pi$. The lower left panel has the same values of $M_{H_2^+}$ and δ but sets $M_{H_3^+} = 500$ GeV. In the lower right panel $M_{H_2^+} = 160$ GeV, $M_{H_3^+} = 170$ GeV, and $\delta = 0.9\pi$. The allowed range of top quark widths from Refs. [28, 29] lies in shaded red area.

where we used $m_b \approx 4$ GeV (using the running bottom quark mass at the weak scale would yield an even higher upper bound on $\tan \beta$). These bounds are generally loose compared to the ranges of $\tan \beta$ usually adopted in collider searches. Nevertheless, we will adapt them to the 3HDM with this in mind. However, the presence of two charged Higgs bosons in the 3HDM makes a direct adaptation of the above analysis rather opaque. Instead, we interpret the constraints as upper bounds on the Yukawa couplings themselves, so that, applied to the 2HDM equivalent of Eq. (2.18), these bounds on $\tan \beta$ are equivalent to imposing $\mathcal{G}_t \lesssim 3.07$ and $\mathcal{G}_b \lesssim 2.90$.

For uniformity we impose $\mathcal{G}_f \lesssim 3$ and derive constraints on $v_1 = v \cos \beta \sin \gamma$, $v_2 = v \sin \beta \sin \gamma$ and $v_3 = v \cos \gamma$ in the Democratic 3HDM using the m_t and m_b values quoted above (plus $m_\tau = 1.78$ GeV). We find

$$\sin \beta \sin \gamma \gtrsim 0.33, \quad \cos \beta \sin \gamma \gtrsim 0.0077, \quad \tan \gamma \lesssim 290. \quad (2.24)$$

The first two constraints yield an absolute lower bound on $\tan \gamma$,

$$\tan \gamma \gtrsim 0.35. \quad (2.25)$$

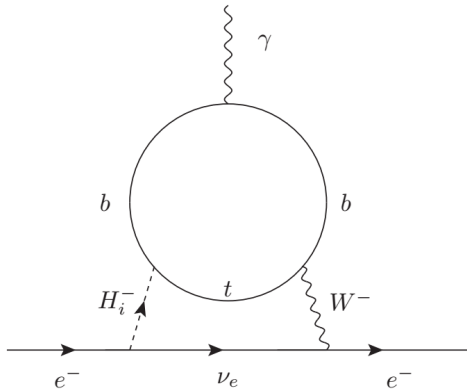


Figure 6. One of the Barr-Zee type diagrams that give the dominant charged Higgs boson contribution to the eEDM in the 3HDM.

Later in this paper, we will show plots for $\tan\gamma = 1$ and 2. For $\tan\gamma = 1$, the perturbativity analysis above requires $0.53 \lesssim \tan\beta \lesssim 92$ and the allowed $\tan\beta$ range expands as $\tan\gamma$ increases.

3 Calculation of EDMs in the 3HDM

In this section, we compute the dominant contributions to the electron and neutron EDMs from CP violation in the charged Higgs sector of the 3HDM. All our results are obtained by a straightforward generalization of the charged Higgs contributions to EDMs that can arise in the 2HDM and are already available in the literature.

3.1 Electron EDM from charged Higgs bosons in the 3HDM

Experimental sensitivity to the eEDM has improved by more than an order of magnitude in recent years, with a current upper bound from the ACME collaboration of [4]:

$$|d_e| \leq 1.1 \times 10^{-29} e \text{ cm (90\% C.L.)}. \quad (3.1)$$

The charged Higgs bosons in the 3HDM give rise to contributions to the eEDM via the CP violation in their couplings to fermion pairs. The one-loop contribution involving a charged Higgs loop is subdominant due to suppression by the tiny electron Yukawa coupling. The dominant contribution comes from the two-loop Barr-Zee type diagrams as shown in Fig. 6, first calculated in Ref. [31] in the 2HDM (see also Ref. [16]).

The charged Higgs sector also appears in the Barr-Zee type diagrams of Fig. 7, where ϕ^0 is any of the neutral scalars in the model. It was pointed out in Ref. [12], in the context of the Aligned 2HDM, that these diagrams can contribute significantly and lead to interesting cancellations with the diagrams of Fig. 6. In the 3HDM scenario that we consider here, where CP violation is present in the charged Higgs sector but not in the neutral Higgs sector

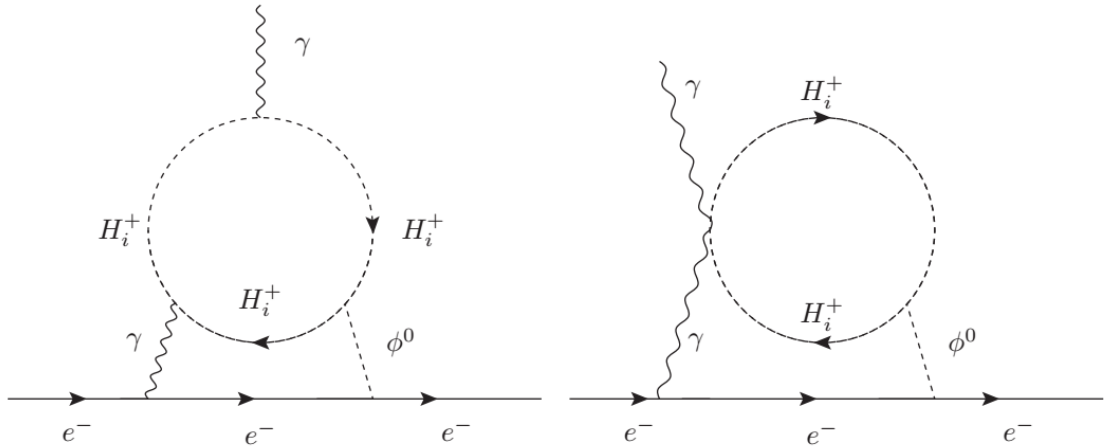


Figure 7. Two of the Barr-Zee type diagrams for the eEDM involving a charged Higgs boson in the loop. These do not contribute in the 3HDM when CP violation is turned off in the neutral Higgs sector, as we assume in this paper.

(which we have integrated out), these diagrams do not contribute to the eEDM because the $\phi^0 ee$ and $\phi^0 H_i^+ H_i^-$ couplings contain no CP phase.¹⁴ The couplings $\phi^0 H_2^+ H_3^-$ do contain non-trivial CP phases, but these couplings do not appear in the diagrams of Fig. 7 because the photon coupling to the charged Higgs boson is diagonal.

Under our assumption that the neutral Higgs sector is CP-conserving and that CP violation appears only in the charged Higgs sector, the dominant Barr-Zee type contribution of the charged Higgs to the eEDM in the 2HDM [16, 31] can be generalized to the 3HDM as follows:

$$\begin{aligned}
\frac{d_e(M_{H_2^\pm}, M_{H_3^\pm})_{BZ}}{2} &= -m_e \frac{12G_F^2 M_W^2}{(4\pi)^4} |V_{tb}|^2 \\
&\times \left[\text{Im}(-Y_2^* Z_2) \left(q_t F_t(z_{H_2^\pm}, z_W) + q_b F_b(z_{H_2^\pm}, z_W) \right) \right. \\
&\left. + \text{Im}(-Y_3^* Z_3) \left(q_t F_t(z_{H_3^\pm}, z_W) + q_b F_b(z_{H_3^\pm}, z_W) \right) \right], \quad (3.2)
\end{aligned}$$

¹⁴It can be seen that, in the absence of neutral (pseudo)scalar sector CP violation, the latter coupling cannot contain a CP-violating phase because this term is Hermitian by itself and hence must have a real coefficient in the Lagrangian.

where $q_t = 2/3$ and $q_b = -1/3$ are quark electric charges, $z_a = M_a^2/m_t^2$ and [16, 31]

$$\begin{aligned}
F_q(z_{H_i^\pm}, z_W) &= \frac{T_q(z_{H_i^\pm}) - T_q(z_W)}{z_{H_i^\pm} - z_W}, \\
T_t(z) &= \frac{1 - 3z\pi^2}{z^2} \frac{1}{6} + \left(\frac{1}{z} - \frac{5}{2}\right) \log z - \frac{1}{z} - \left(2 - \frac{1}{z}\right) \left(1 - \frac{1}{z}\right) \text{Li}_2(1 - z), \\
T_b(z) &= \frac{2z - 1}{z^2} \frac{\pi^2}{6} + \left(\frac{3}{2} - \frac{1}{z}\right) \log z + \frac{1}{z} - \frac{1}{z} \left(2 - \frac{1}{z}\right) \text{Li}_2(1 - z).
\end{aligned} \tag{3.3}$$

Note that the original calculation of Ref. [31] was done setting $m_b = 0$ so that only the contribution involving the top-quark Yukawa couplings $m_t Y_i/v$ appears. Keeping the non-zero bottom mass would introduce additional contributions proportional to $m_b X_i/v$, which could become important at large values of $\tan\beta$. Finally, all other eEDM contributions at the loop level that are purely fermionic or induced by gauge bosons [32, 33] remain identical to those in the SM and are negligible compared to the current experimental bound.

3.2 Neutron EDM from charged Higgs bosons in the 3HDM

The current measurement of the nEDM at the Paul Scherrer Institute with ultra-cold neutrons (UCN) provided an upper limit as follows [3]:¹⁵

$$|d_n| \leq 1.8 \times 10^{-26} e \text{ cm (90\% C.L.)}. \tag{3.4}$$

CP violation from charged Higgs boson exchange enters this observable through a variety of effective operators. Jung and Pich [16] point out three types of effective operators through which the charged Higgs boson contributes to the nEDM in the 2HDM. These are four-fermion operators involving the up- and down-type quarks which are induced by CP-violating Higgs exchange, the Weinberg operator (the CP-violating three-gluon operator) which is neither suppressed by quark masses nor CKM matrix elements, and the Barr-Zee type two-loop diagrams contributing to the EDMs and chromo-electric dipole moments (CEDMs) of the up- and down-type quarks. The light quark masses suppress the contributions of the four fermion operators and the up- and down-type quark (C)EDMs.

This leaves the Weinberg operator, the charged Higgs contribution to which is shown in the left panel of Fig. 8. Following Ref. [16], we compute this using an effective field theory approach [35], which amounts to computing only the one-loop short-distance piece at the high scale $\mu_{tH} = m_t$, which is the bottom quark CEDM shown in the right panel of Fig. 8.

The contribution of the Weinberg operator to the nEDM is [16]:

$$|d_n(C_W)/e| = \left[\begin{array}{c} 1.0 \\ -0.5 \end{array} \begin{array}{c} +1.0 \\ -0.5 \end{array} \right] \times 20 \text{ MeV } C_W(\mu_h), \tag{3.5}$$

where the sign is unknown, and the theoretical uncertainty on the magnitude is a factor of two. In our numerical results, we follow Ref. [16] and use the central theoretical value. The

¹⁵If the (unrealistic) assumption is made that the nEDM is the sole contribution to the atomic EDM of mercury, the most recent measurement of the latter yields a comparable limit, $|d_n| < 1.8 \times 10^{-26} e \text{ cm}$ at 90% C.L. [34].

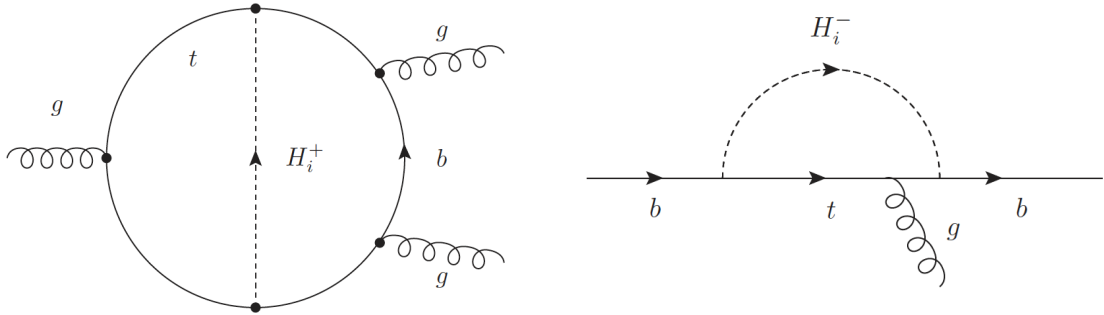


Figure 8. Left panel: Two-loop charged Higgs boson contribution to the Weinberg operator. Right panel: One-loop charged Higgs boson contribution to the bottom quark CEDM.

Wilson coefficient C_W evaluated at the hadronic scale $\mu_h \sim 1$ GeV is expressed as

$$C_W(\mu_h) = \eta_{c-h}^{\kappa_W} \eta_{b-c}^{\kappa_W} \left(\eta_{t-b}^{\kappa_W} C_W(\mu_{tH}) + \eta_{t-b}^{\kappa_C} \frac{g_s^3(\mu_b)}{8\pi^2 m_b} \frac{d_b^C(\mu_{tH})}{2} \right), \quad (3.6)$$

where $C_W(\mu_{tH}) = 0$ because there is no short-distance contribution to the Weinberg operator involving the charged Higgs boson at the scale m_t . $d_b^C(\mu_{tH})$ is the short-distance contribution to the bottom quark CEDM, given below. The running of these short-distance contributions down to the scale $\mu_b = m_b$ is accomplished by the factors of $\eta_{t-b} = \alpha_s(\mu_{tH})/\alpha_s(\mu_b)$ raised to the appropriate power $\kappa_i = \gamma_i/(2\beta_0)$, where $\gamma_W = N_C + 2n_f$ and $\gamma_C = 10C_F - 4N_C$ are the leading order (LO) anomalous dimensions of the Weinberg and b -quark CEDM operator, respectively, and $\beta_0 = (11N_C - 2n_f)/3$ is the one-loop beta function of QCD. Here, $N_C = 3$, $C_F = 4/3$, and n_f is the number of active quark flavors involved in the QCD running at the relevant scale (e.g., between the top and bottom masses, $n_f = 5$). At the scale μ_b , the bottom quark is integrated out and the operators matched, then the remaining Weinberg operator is run down to the hadronic scale μ_h in two steps (integrating out the charm quark at $\mu_c = m_c$), giving rise to two more factors, $\eta_{b-c}^{\kappa_W}$ and $\eta_{c-h}^{\kappa_W}$, in which the running of α_s and the exponent are evaluated with the appropriate value of n_f . At LO, $\alpha_s(\mu)$ is given by:

$$\alpha_s(\mu) = \frac{\alpha_s(M_Z)}{v(\mu)}, \quad (3.7)$$

with

$$v(\mu) = 1 - \beta_0 \frac{\alpha_s(M_Z)}{2\pi} \log\left(\frac{M_Z}{\mu}\right). \quad (3.8)$$

Finally, the high-scale one-loop charged Higgs boson contribution to the bottom quark CEDM in the right panel of Fig. 8 has been calculated in the 2HDM in Ref. [16] (see also references therein). By adapting this to the 3HDM, one obtains

$$\begin{aligned} \frac{d_b^C(\mu_{tH})}{2} = & -\frac{G_F}{\sqrt{2}} \frac{1}{16\pi^2} |V_{tb}|^2 m_b(\mu_{tH}) \left[\text{Im}(-X_2 Y_2^*) x_{tH_2} \left(\frac{\log(x_{tH_2})}{(x_{tH_2} - 1)^3} + \frac{(x_{tH_2} - 3)}{2(x_{tH_2} - 1)^2} \right) \right. \\ & \left. + \text{Im}(-X_3 Y_3^*) x_{tH_3} \left(\frac{\log(x_{tH_3})}{(x_{tH_3} - 1)^3} + \frac{(x_{tH_3} - 3)}{2(x_{tH_3} - 1)^2} \right) \right], \quad (3.9) \end{aligned}$$

where $x_{tH_i} = m_t^2/M_{H_i^\pm}^2$. Again, purely fermionic and gauge contributions [16] remain identical to those in the SM and are negligible compared to the current experimental bound.

4 Cancellation in the charged Higgs contributions to the EDMs

The CP-violating phase in the charged Higgs mixing matrix is responsible for generating CP-violating observables in this model. The effects of this CP-violating phase in processes involving virtual charged Higgs boson exchange can be arbitrarily suppressed by making the two physical charged Higgs bosons sufficiently degenerate in mass, thereby avoiding constraints from EDMs. This can be understood as a consequence of an analogue of the GIM mechanism [13], in particular, when H_2^\pm and H_3^\pm become degenerate, both the mixing angle θ and the CP-violating phase δ in their mixing matrix become non-physical.

Any internal charged Higgs propagator that begins and ends on a fermion line brings with it one factor of X_i^* , Y_i^* or Z_i^* and one factor of X_i , Y_i or Z_i . The combinations $X_i X_i^*$, $Y_i Y_i^*$, and $Z_i Z_i^*$ are purely real and cannot contribute to CP-odd observables, leaving only the combinations $X_i Y_i^*$, $X_i Z_i^*$ and $Y_i Z_i^*$ (or their complex conjugates) which can have an imaginary part. Consider, for example, $X_i Y_i^*$, which is given in the Democratic 3HDM in terms of the unitary rotation matrix in Eq. (2.17) by

$$X_i Y_i^* = -\frac{U_{1i}^\dagger U_{i2}}{U_{11}^\dagger U_{12}}, \quad (4.1)$$

where $i = 2$ or 3 . The denominator is real by construction since $U_{1j} = v_j/v$. Computation of CP-odd observables in this context always involves a sum over the two charged Higgs bosons that can appear in the contributing diagrams, yielding

$$\sum_{i=2}^3 \text{Im}(X_i Y_i^*) f(M_{H_i^\pm}) = -\frac{1}{U_{11}^\dagger U_{12}} \left[\text{Im}(U_{12}^\dagger U_{22}) f(M_{H_2^\pm}) + \text{Im}(U_{13}^\dagger U_{32}) f(M_{H_3^\pm}) \right], \quad (4.2)$$

where $f(M_{H_i^\pm})$ represents the dependence of the diagram on the charged Higgs boson mass. We can trivially add zero in the form of $\text{Im}(U_{11}^\dagger U_{12}) f(m)$ inside the square brackets. Then, in the limit $M_{H_2^\pm} = M_{H_3^\pm} \equiv m$, Eq. (4.2) becomes

$$\sum_{i=2}^3 \text{Im}(X_i Y_i^*) f(m) = -\frac{1}{U_{11}^\dagger U_{12}} \text{Im} \left[\sum_{i=1}^3 U_{1i}^\dagger U_{i2} \right] f(m) = -\frac{1}{U_{11}^\dagger U_{12}} \text{Im}(\delta_{12}) f(m) = 0, \quad (4.3)$$

where δ_{12} is the (1, 2) element of the Kronecker delta. This also shows that $\text{Im}(X_2 Y_2^*) = -\text{Im}(X_3 Y_3^*)$, due to the unitarity of the charged Higgs mixing matrix, and similarly for the imaginary parts of $X_i Z_i^*$ and $Y_i Z_i^*$. The form of Eq. (4.2) also implies that, for small non-zero mass splitting $\Delta M_{H^\pm} \ll M_{H^\pm}$, CP-violating amplitudes must be linear in $\Delta M_{H^\pm}/M_{H^\pm}$, where $\Delta M_{H^\pm} \equiv M_{H_3^\pm} - M_{H_2^\pm}$ and $M_{H^\pm} \equiv (M_{H_3^\pm} + M_{H_2^\pm})/2$.¹⁶

¹⁶The degeneracy of the charged Higgs boson masses favored by the avoidance of EDM constraints raises the possibility of interesting interference effects in direct collider production of on-shell charged Higgs

In this paper, we focus on the Democratic 3HDM because CP violation in the charged Higgs sector gives rise to interesting contributions to the EDMs of both the electron and neutron. In the other types of 3HDM, the effects of charged Higgs CP violation are more limited because, in these models, at least two of X_i , Y_i , and Z_i become identical (see Tab. 2). In particular, the dominant charged Higgs contribution to the eEDM, proportional to $\text{Im}(-Y_i^* Z_i)$, is zero in the Type-I and Type-Y (Flipped) 3HDMs because in those models $Y_i = Z_i$. Similarly, the dominant charged Higgs contribution to the nEDM, proportional to $\text{Im}(-X_i Y_i^*)$, is zero in the Type-I and Type-X (Lepton-specific) 3HDMs because in those models $X_i = Y_i$. In the Type-II 3HDM, $X_i = Z_i$, so that this model also leads to CP-violating charged Higgs boson contributions to both the electron and neutron EDMs.

5 Numerical results

We now present our results for the Democratic 3HDM as a function of the relevant coupling parameters (θ , $\tan\beta$, $\tan\gamma$, and δ) and masses ($M_{H_2^\pm}$ and $M_{H_3^\pm}$) against the eEDM and nEDM constraints. We will also impose the constraints from direct searches for charged Higgs bosons, as well as from the measurement of $\text{BR}(\bar{B} \rightarrow X_s \gamma)$, which provides the most stringent indirect constraint on the charged Higgs masses. Details of our implementation of the $\bar{B} \rightarrow X_s \gamma$ constraint are given in Appendix A.

To start with, it is instructive to compare the 3HDM results with those available in the literature for the analogous case in a 2HDM, which we do by presenting the nEDM and eEDM constraints against the Yukawa coupling combinations $\text{Im}(X_i Y_i^*)$ and $\text{Im}(Y_i^* Z_i)$ ($i = 2$). In Fig. 9, we show the Aligned 2HDM results in the plane of the charged Higgs mass and the imaginary part of the relevant combination of Yukawa coupling factors, to be compared to Figs. 3, 4, and 5 of Ref. [16],¹⁷ updated using the latest nEDM and eEDM experimental limits as given in Eqs. (3.4) and (3.1), respectively. The shaded areas in Fig. 9 represent the viable parameter regions in both cases. The newest bounds from both nEDM and eEDM induce a strong suppression on the allowed parameter space corresponding to the imaginary contributions of the couplings $X_2 Y_2^*$ and $Y_2^* Z_2$. In Figs. 10 and 11, we show the 3HDM cases as a function of $M_{H_2^\pm}$ with $M_{H_3^\pm} = 85$ and 300 GeV, respectively. We can then see that the parameter space is generally enlarged in the Democratic 3HDM with respect to the Aligned 2HDM, particularly in the $M_{H_2^\pm} = M_{H_3^\pm}$ limit, clearly illustrating

bosons, if their mass splitting is comparable to or smaller than the decay widths of the two charged Higgs bosons so that the BW lineshapes of their decay products overlap in phase space. Unfortunately, for the case when both charged Higgs boson masses are below m_t , not only are their decay widths extremely narrow (as illustrated already), but it is also very difficult (maybe impossible) to find a viable set of model parameters that are not already ruled out by collider searches for which such a degeneracy can be achieved. For charged Higgs boson masses above m_t , however, collider constraints are much less stringent and the decay widths are larger, so that such a lineshape overlap could offer interesting future possibilities for experimental exploration. For example, for the set of values in Fig. 17, the width of H_3^\pm is of the order of 1 GeV when $M_{H_2^\pm} = M_{H_3^\pm} = 200$ GeV and of the order of 10^2 GeV for $M_{H_2^\pm} = M_{H_3^\pm} = 800$ GeV whereas the width of H_2^\pm is of the order of 10^{-3} GeV when $M_{H_2^\pm} = M_{H_3^\pm} = 200$ GeV and of the order of 0.1 GeV for $M_{H_2^\pm} = M_{H_3^\pm} = 800$ GeV.

¹⁷Herein, there is no subscript 2 for the couplings and masses of the 2HDM, as only one charged Higgs state is present in the model.

the aforementioned cancellation mechanism between the two charged Higgs states of the 3HDM. It is worth noticing here that, while in the exact mass degeneracy case there is virtually no constraint applicable to the Democratic 3HDM from either nEDM or eEDM, even when the $M_{H_2^\pm} = M_{H_3^\pm}$ condition is lifted, there are substantial differences in the values allowed for the Yukawa couplings between the two scenarios at both small and large values of the lightest charged Higgs boson mass.

Next, we consider the effect of the coupling parameters θ , $\tan\beta$, $\tan\gamma$, and δ for various scenarios for the charged Higgs masses $M_{H_2^\pm}$ and $M_{H_3^\pm}$ within the Democratic 3HDM. We consider two classes of mass scenarios: the first in which either or both H_i^\pm masses are lighter than m_t (in Sec. 5.1) and the second in which they are both heavier than m_t (in Sec. 5.2). Explicit expressions for the parameter combinations $\text{Im}(-X_2 Y_2^*)$ and $\text{Im}(-Y_2^* Z_2)$ that enter the calculations of the EDMs are given in Appendix B; in particular we note that these quantities are proportional to $\sin\delta$ and to the product $\sin\theta\cos\theta$, so that the CP-violating effects are largest when $\delta = \pi/2$ or $3\pi/2$ and $\theta = -\pi/4$.

5.1 Light charged Higgses

5.1.1 The $M_{H_2^\pm} < m_t < M_{H_3^\pm}$ case

In Fig. 12, we show the constraints from $\bar{B} \rightarrow X_s \gamma$, eEDM and nEDM on the $[\delta, \theta]$ plane, for $M_{H_2^+} = 80$ GeV, $M_{H_3^+} = 200$ GeV, and small values of $\tan\beta$ and $\tan\gamma$ so as to be compliant with collider limits, as seen previously. Notice that the $\bar{B} \rightarrow X_s \gamma$ constraint is satisfied within the green and grey shaded areas while the two EDM constraints are satisfied outside the corresponding closed curves. (Details of our calculation of the $\bar{B} \rightarrow X_s \gamma$ constraint are given in Appendix A.) The shaded areas correspond to the $\pm 2\sigma$ allowed region of $\text{BR}(\bar{B} \rightarrow X_s \gamma)$, with the green (grey) area corresponding to values below (above) the experimental central value. From these plots, we learn that we need δ to be very close to $\delta = n\pi$ to satisfy all three constraints at once. That is, we are forced to find solutions very close to the CP-conserving limit; furthermore, the constraint from $\bar{B} \rightarrow X_s \gamma$ furthermore tends to favour $\delta \simeq \pi$.

In Fig. 13, we show the effect of varying $\tan\gamma$ and increasing the mass of the heavier charged Higgs state while keeping $M_{H_2^\pm} = 80$ GeV and fixing $\tan\beta = 20$. As can be seen, increasing $M_{H_3^\pm}$ from 200 to 500 GeV makes it more difficult to find regions that can survive all constraints, in line with the requirements of the aforementioned cancellation mechanism. Comparing with Fig. 12 we also see that larger values of $\tan\beta$ lead to tighter constraints from the nEDM while larger values of $\tan\gamma$ lead to tighter constraints from the eEDM.

In Fig. 14, we show the same constraints on the $[\tan\gamma, \tan\beta]$ plane instead, for $\theta = -0.3$ and two characteristic values of δ chosen to be very close to π , i.e., $\delta = 0.975\pi$ and 0.985π . We have also added here the constraints from the top-quark width and perturbativity of the $H_i^+ b\bar{t}$ vertex. The allowed region is the portion of the green and grey shaded areas that lies to the right of the black dotted line and above the blue curve. For all the parameter regions shown, the collider limits are satisfied. We can see that, for $\tan\gamma > 1.5$ and $\tan\beta > 8$, we can satisfy all other constraints for these values of δ .

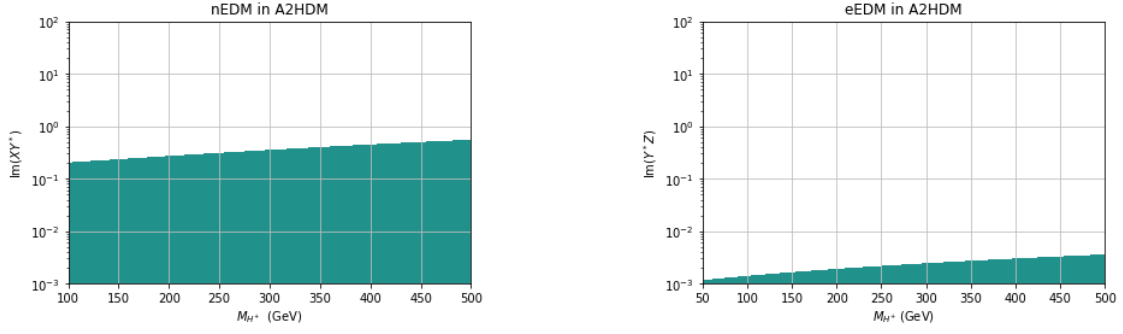


Figure 9. Constraint from the nEDM (left) and the eEDM (right) on $|\text{Im}(XY^*)|$ and $|\text{Im}(Y^*Z)|$, respectively, in the Aligned 2HDM as a function of the charged Higgs mass (M_{H^+}). The blue shaded region is allowed.

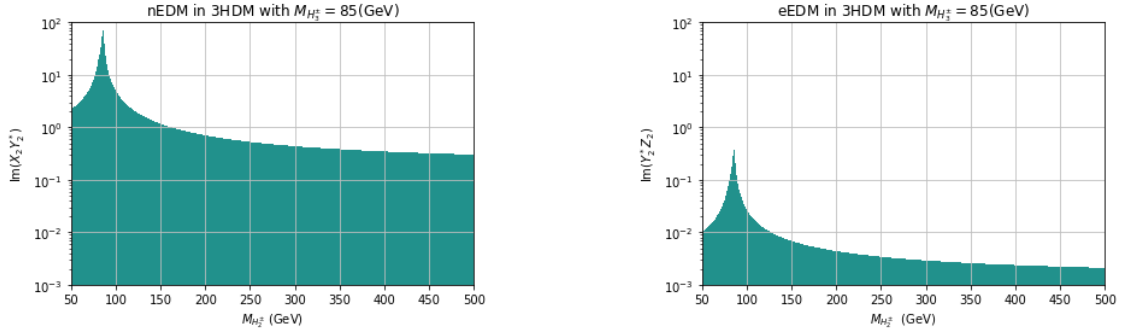


Figure 10. Constraint from the nEDM (left) and the eEDM (right) on $|\text{Im}(X_2 Y_2^*)|$ and $|\text{Im}(Y_2^* Z_2)|$ in the 3HDM as a function of the mass of H_2^+ . $M_{H_2^+}$ is fixed to be 85 GeV. The structure of the model forces $\text{Im}(X_3 Y_3^*) = -\text{Im}(X_2 Y_2^*)$ and $\text{Im}(Y_3^* Z_3) = -\text{Im}(Y_2^* Z_2)$.

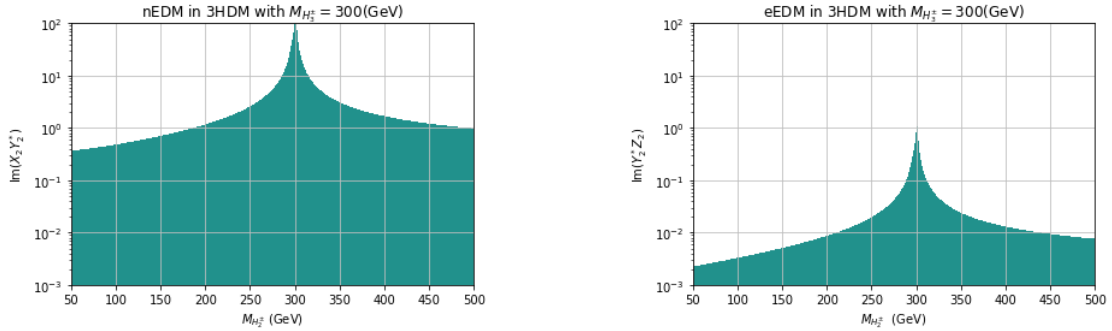


Figure 11. Same as in Fig. 10 but for $M_{H_3^\pm} = 300$ GeV.

5.1.2 The $M_{H_2^\pm} < M_{H_3^\pm} < m_t$ case

Similarly to the previous case, also here we need low values of $\tan\beta$ to satisfy the top-quark width measurements. However, this is in tension with the region of parameter space that

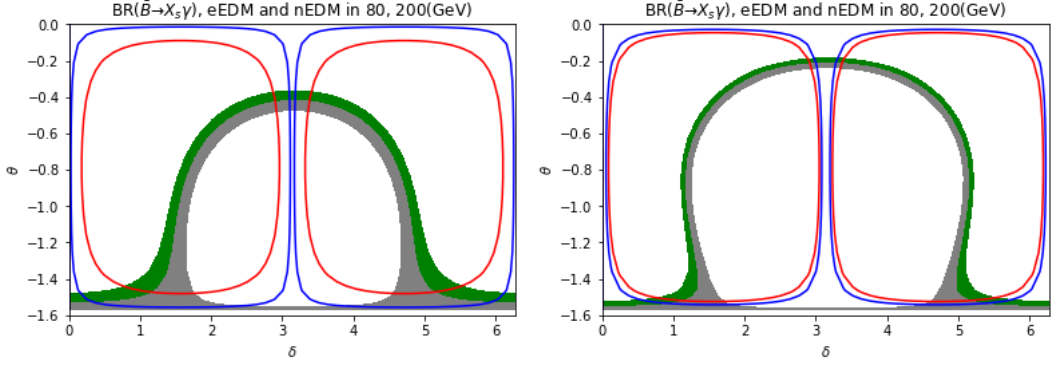


Figure 12. The allowed regions from $\bar{B} \rightarrow X_s \gamma$ (within the green and grey shaded areas), eEDM (outside the blue curves), and nEDM (outside the red curves) in the $[\delta, \theta]$ plane, with $M_{H_2^+} = 80$ GeV, $M_{H_3^+} = 200$ GeV, $\tan \gamma = 1$, and $\tan \beta = 5$ (left) or 10 (right). Here, the shaded areas correspond to the $\pm 2\sigma$ allowed region of $\text{BR}(\bar{B} \rightarrow X_s \gamma)$, with the green (grey) area corresponding to values below (above) the experimental central value.

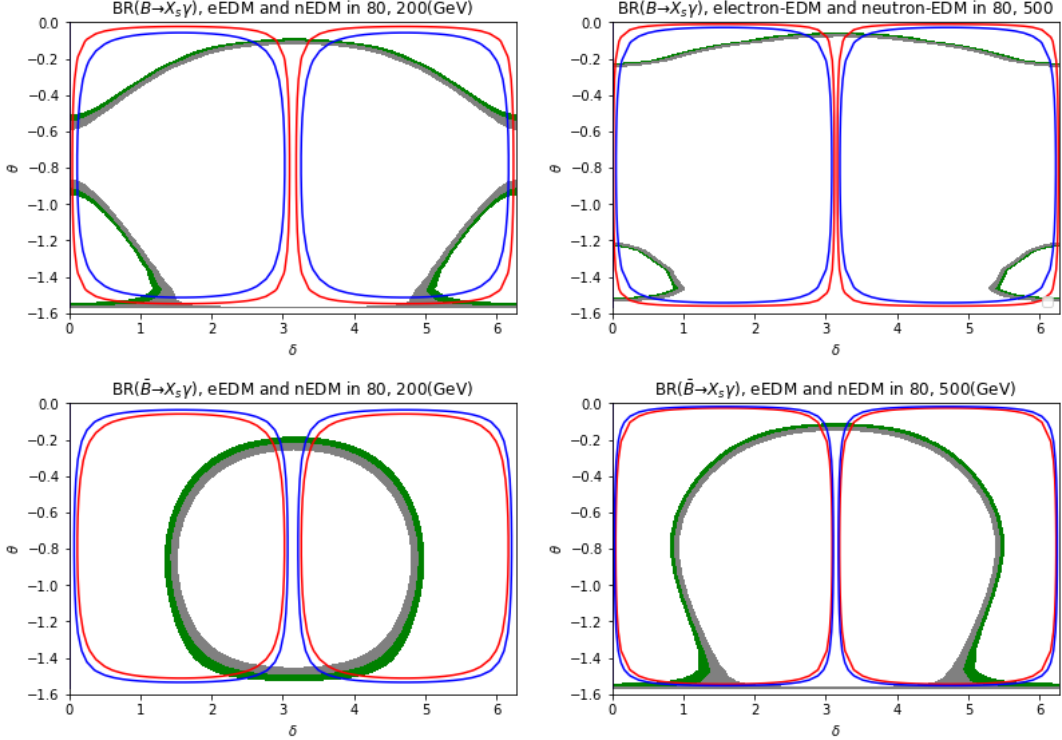


Figure 13. The allowed regions from $\bar{B} \rightarrow X_s \gamma$ (within the green and grey shaded areas), eEDM (outside the blue curves), and nEDM (outside the red curves) in the $[\delta, \theta]$ plane, with $M_{H_2^+} = 80$ GeV and $\tan \beta = 20$. $M_{H_3^+} = 200$ GeV in the left panels and 500 GeV in the right panels. Here, $\tan \gamma = 1$ in the upper panels and 2 in the lower panels.

satisfies simultaneously the constraints from $\bar{B} \rightarrow X_s \gamma$, eEDM, and nEDM, despite which, as can be seen in Fig. 15, we could have a somewhat wider interval of δ around π for large

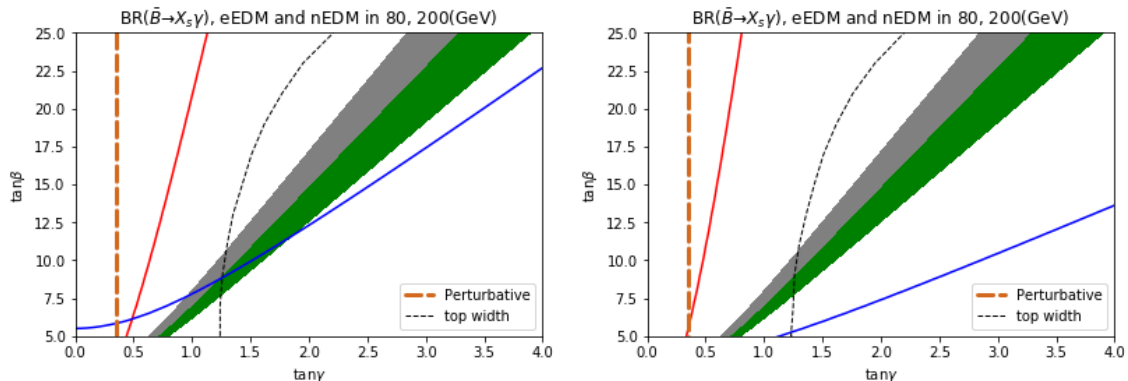


Figure 14. The allowed regions from $\bar{B} \rightarrow X_s \gamma$ (within the green and grey shaded areas), eEDM (above the blue line) and nEDM (to the right of the red line) in the $[\tan \gamma, \tan \beta]$ plane, with $M_{H_2^\pm} = 80$ GeV, $M_{H_3^\pm} = 200$ GeV, $\theta = -0.3$, and $\delta = 0.975\pi$ (left) or 0.985π (right). We also show constraints from the top-quark width (black dotted line) and perturbativity (orange dashed line), wherein the region to the right of the respective curves is allowed.

values of $\tan \beta$ and $\tan \gamma$. There also seems to be a broader band satisfying the $\bar{B} \rightarrow X_s \gamma$ constraint for lower values of $M_{H_3^\pm}$, while keeping $M_{H_2^\pm} = 80$ GeV. This, again, is in tension with the aforementioned experimental constraints. However, in this case, it is the collider limit on $H^\pm \rightarrow \tau \nu$ that becomes too restrictive on the H_3^\pm properties as we decrease its mass. But we can prevent this from happening if we keep $M_{H_3^\pm} = 170$ GeV and increase instead the mass of $M_{H_2^\pm}$, which is what we do in Fig. 16. In the upper panel of this figure, we show the case $M_{H_2^\pm} = 80$ GeV and $M_{H_3^\pm} = 170$ GeV. In this case, the top-quark width measurement is very constraining, and very low values of $\tan \gamma$ are ruled out. In the lower panel of this figure, we show the case $M_{H_2^\pm} = 160$ GeV and $M_{H_3^\pm} = 170$ GeV. Here, the top-quark width measurement is not that constraining, and very low values of $\tan \gamma$ are allowed. With the two charged Higgs masses closer to being degenerate, a larger range of the CP-violating phase δ also becomes allowed.

5.2 Heavy charged Higgses

In the case that both the H_2^\pm and H_3^\pm masses are heavier than the top-quark mass, collider searches no longer significantly limit the parameter space, so we present the $\bar{B} \rightarrow X_s \gamma$, eEDM and nEDM constraints on the $[M_{H_2^\pm}, M_{H_3^\pm}]$ plane with different choices for the mixing parameters ($\tan \beta$, $\tan \gamma$, θ , and δ). We choose the parameters $\theta = -0.476\pi$ ($-\pi/4$), $\tan \beta = 20$ (40) and $\tan \gamma = 1$ (2) to plot from Fig. 17 to Fig. 22. Specifically, Figs. 17–19 are plotted for three different δ values for the same $\theta = -0.476\pi$, where $\delta = 0.5\pi$ (maximum CP-violating scenario), 0.85π , and 0.9π (two choices closer to the CP-conserving limit). In Fig. 17, the two bottom panels clearly show that the most constraining limit comes from the nEDM when $\tan \beta = 40$. For the choice of $\tan \beta = 20$ and $\tan \gamma = 2$, the top right panel shows instead that the eEDM constraint is the one limiting most of the parameter space. In Figs. 18 and 19, a large expanse of parameter space is allowed by both the eEDM and nEDM constraints. In fact, here, EDM constraints no longer strictly limit the parameter

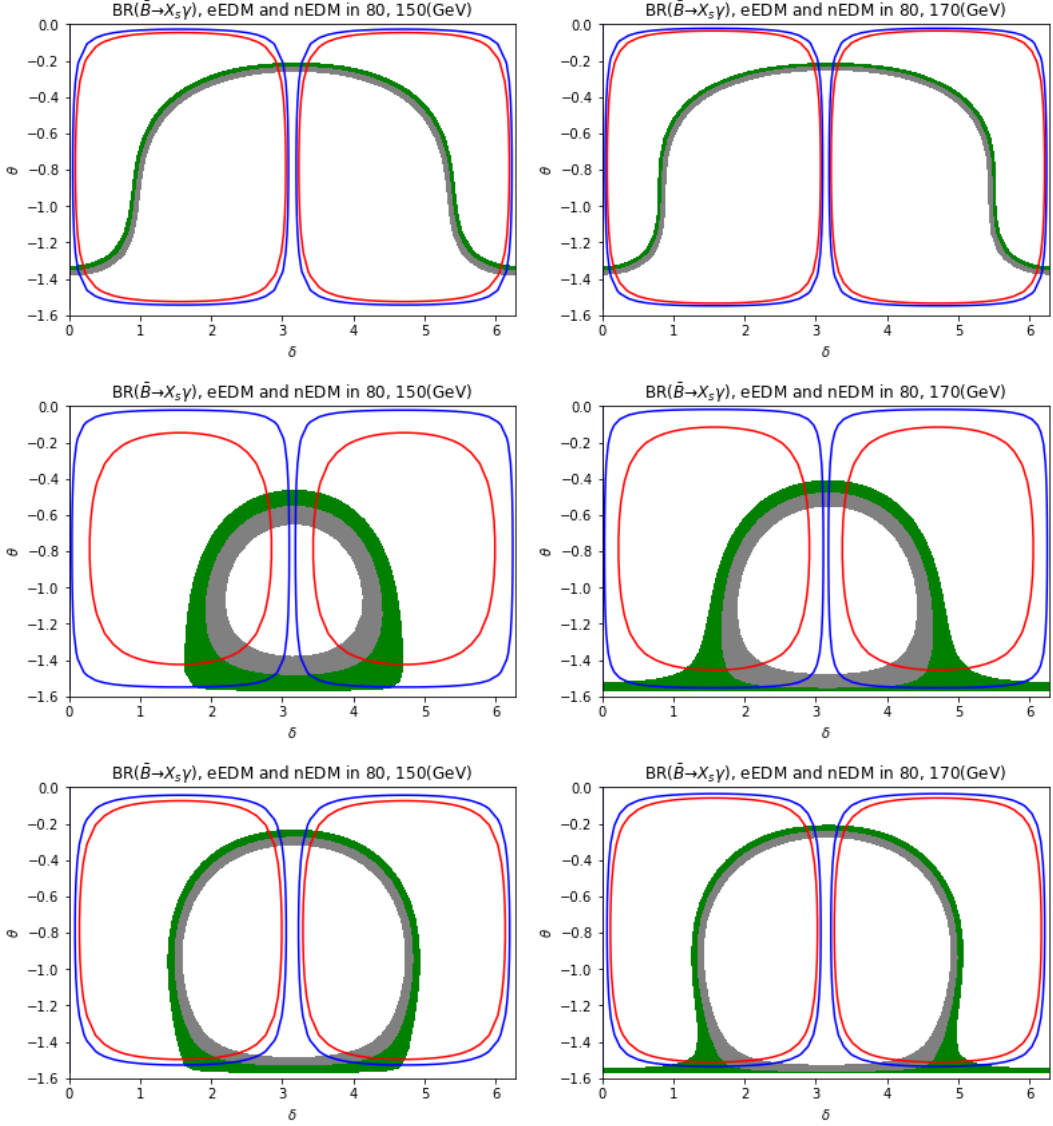


Figure 15. The allowed regions from $\bar{B} \rightarrow X_s \gamma$ (within the green and grey shaded areas), eEDM (outside the blue curves), and nEDM (outside the red curves) in the $[\delta, \theta]$ plane, with $M_{H_2^+} = 80$ GeV and $M_{H_3^+} = 150$ (left) or 170 (right) GeV. From top to bottom, $(\tan \beta, \tan \gamma) = (5, 0.5)$; $(5, 1)$; and $(10, 1)$.

space so that $\bar{B} \rightarrow X_s \gamma$ becomes the essential constraint, especially as δ gets close to π . The typical funnel shape of the allowed region along the mass diagonal for the EDM constraints illustrates again the impact of the GIM-like cancellation mechanism driven by the charged Higgs mass degeneracy, the more so the smaller their absolute values. Such a cancellation is not present in the $\bar{B} \rightarrow X_s \gamma$ constraint, since this observable receives both real and imaginary contributions from $X_i Y_i^*$ terms, with the real components of $X_2 Y_2^*$ and $X_3 Y_3^*$ not being strongly correlated as their imaginary parts are; the corresponding shape thus departs from the funnel one and depends more on a judicious choice of θ for given values

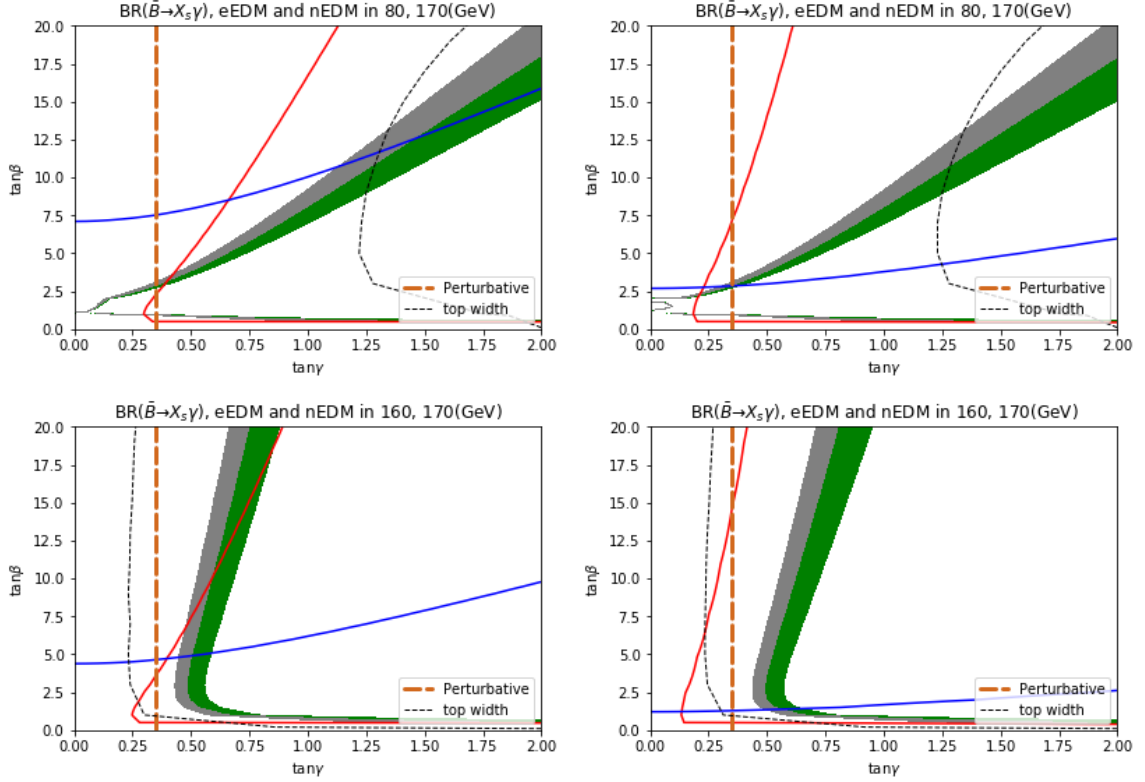


Figure 16. The allowed regions from $\bar{B} \rightarrow X_s \gamma$ (within the green and grey shaded areas), eEDM (above the blue line), and nEDM (to the right of the red line) in the $[\tan \gamma, \tan \beta]$ plane, with $M_{H_3^+} = 170$ GeV. In the upper panels $M_{H_2^+} = 80$ GeV, $\theta = -0.3$, and $\delta = 0.96\pi$ (left) or 0.985π (right). In the lower panels $M_{H_2^+} = 160$ GeV, $\theta = -0.5$, and $\delta = 0.8\pi$ (left) or 0.95π (right). We also show constraints from the top-quark width (black dotted line) and perturbativity (orange dashed line), wherein the region to the right of the respective curves is allowed.

of $\tan \beta$ and $\tan \gamma$.

In the case of $\theta = -\pi/4$, three similar figures, Figs. 20, 21, and 22, are presented for $\delta = 0.5\pi, 0.85\pi$ and 0.9π , respectively. For this θ value, it is intriguing to note that even the exact degeneracy case between H_2^\pm and H_3^\pm fails the $\bar{B} \rightarrow X_s \gamma$ constraint for the smallest δ choice. In contrast, for the other δ values, the main effect is a significant restriction of the parameter space allowed by $\bar{B} \rightarrow X_s \gamma$ along the $M_{H_2^\pm} = M_{H_3^\pm}$ diagonal while, conversely, the EDM constraints are less invasive. This is a generalized feature quite irrespectively of the value of $\tan \beta$, so long as $\tan \gamma$ remains small.

6 Conclusions

In this paper, we have studied a version of the 3HDM, called Democratic, wherein each amongst the down-type quarks, up-type quarks, and charged leptons gain their mass from one only of the three VEVs of the Higgs doublets, in the presence of explicit CP violation in the charged Higgs sector, which consists of two physical states, each with mass varying

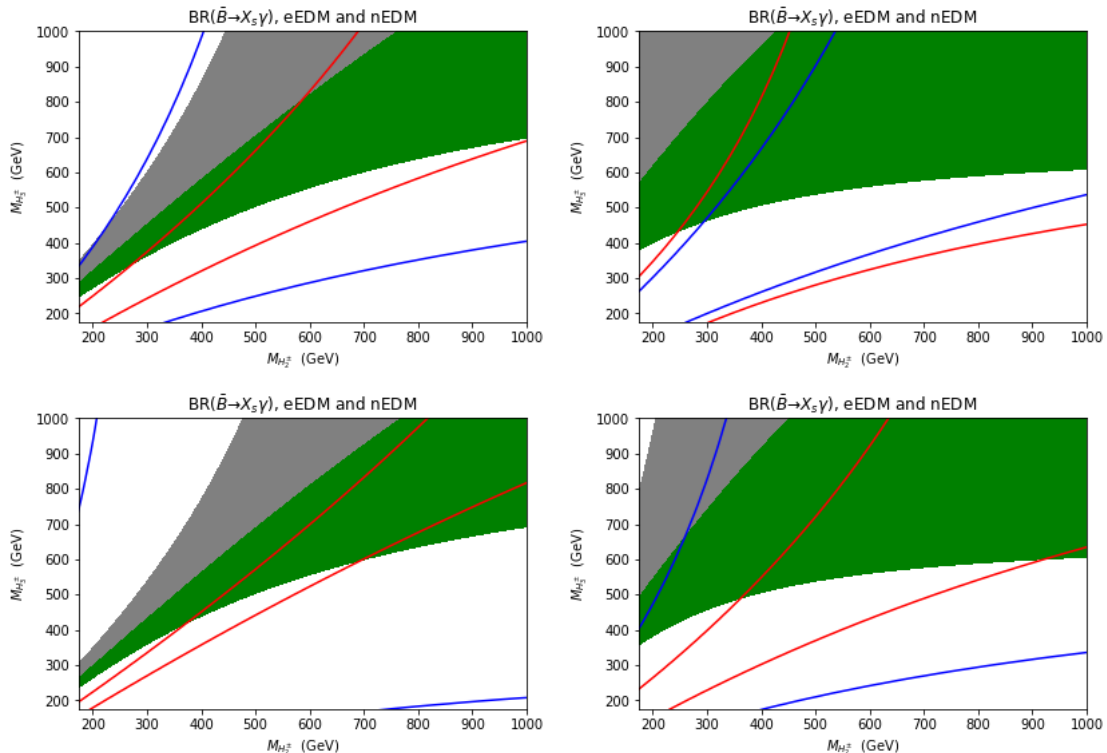


Figure 17. The allowed regions from $\bar{B} \rightarrow X_s \gamma$ (within the green and grey shaded areas), eEDM (between the blue lines), and nEDM (between the red lines) in the $[M_{H_2^\pm}, M_{H_3^\pm}]$ plane, for $\theta = -0.476\pi$ and $\delta = 0.5\pi$ (i.e., maximal CP violation), with $\tan\beta = 20$ (upper panels) or 40 (lower panels) and $\tan\gamma = 1$ (left panels) or 2 (right panels).

from 80 GeV to the TeV scale. While an enlarged neutral Higgs sector also exists in this framework, consisting, in addition to the SM-like Higgs state already discovered, of four other neutral Higgs states, two CP-even and two CP-odd, these have been assumed to be sufficiently heavy compared to the charged Higgs bosons so as to not significantly affect the low energy phenomenology of the 3HDM. In particular, we showed that it is possible to isolate the effects of CP violation to the charged Higgs sector only, and derived the conditions on the complex parameters of the scalar potential required to achieve this. We have studied the charged Higgs sector in terms of the following experimental observables, all very sensitive to new CP-violating effects emerging alongside those contained in the CKM matrix: $\text{BR}(\bar{B} \rightarrow X_s \gamma)$, eEDM, and nEDM.

We have tested the parameter space of the 3HDM, mapped in terms of the two charged Higgs boson masses $M_{H_2^\pm}$ and $M_{H_3^\pm}$ and four parameters entering their Yukawa couplings, $\tan\beta$, $\tan\gamma$, θ , and the CP violating phase δ , against experimental measurements of these three observables. In doing so, we have discovered a sort of GIM-like cancellation mechanism between the two charged Higgs contributions to eEDM and nEDM driven by the unitarity of the charged Higgs mixing matrix.¹⁸ Such a cancellation becomes exact when $M_{H_2^\pm} =$

¹⁸An equivalent cancellation occurs in the CP-odd asymmetries in $\bar{B} \rightarrow X_s \gamma$, considered in Ref. [36].

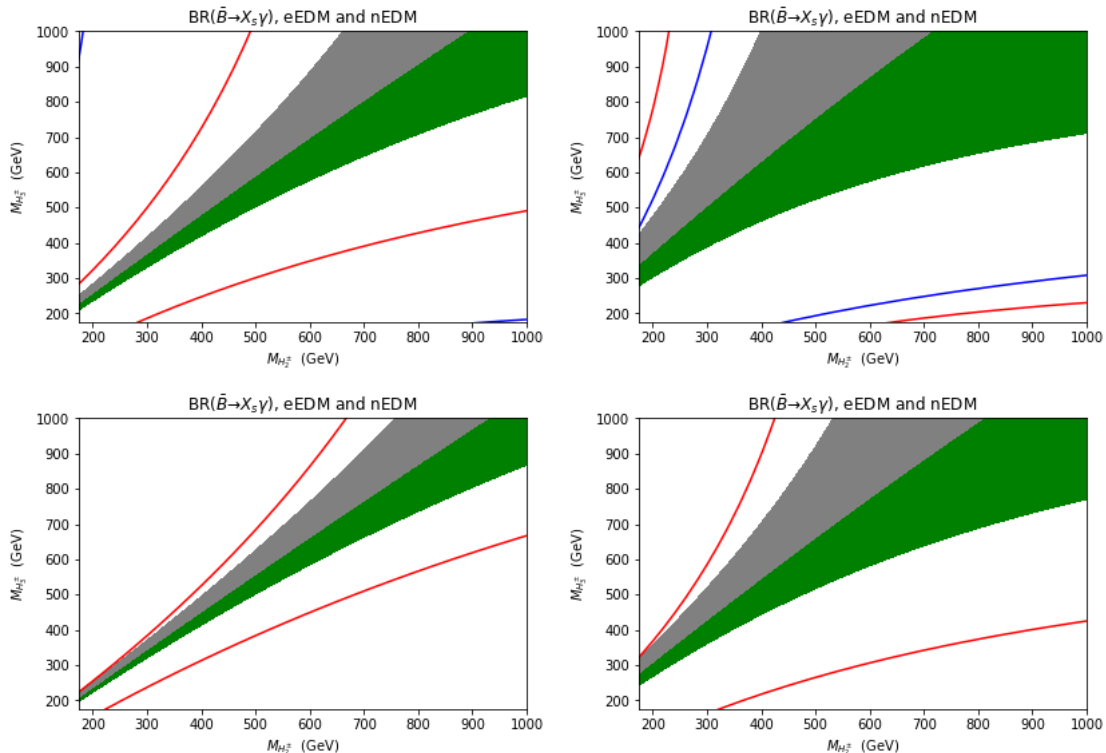


Figure 18. Same as Fig. 17 but with $\delta = 0.85\pi$.

$M_{H_3^\pm}$. As a consequence, it is then possible to evade the experimental constraints enforced through the aforementioned CP-odd observables whichever the values of $\tan\beta$, $\tan\gamma$, θ , and δ .

Even in less fine-tuned conditions, when we lift the charged Higgs boson mass degeneracy, interesting phenomenology emerges. Specifically, light H_2^\pm and/or H_3^\pm states, with mass below m_t , are still allowed not only by the $\text{BR}(\bar{B} \rightarrow X_s \gamma)$, eEDM and nEDM constraints but also by those induced by the experimental measurements of the top quark decay width and direct searches for top quark decays to charged Higgs bosons with subsequent charged Higgs decays to $\tau^+ \nu$, $c\bar{s}$, and $c\bar{b}$ at the LHC, as well as the theoretical requirement of perturbativity of the Yukawa couplings. While this is really only possible near the CP-conserving limit and when the lightest of the two charged Higgs states has a mass close to M_W (so as to be unconstrained by the LHC, owing to the overwhelming irreducible W^\pm background herein), also for small values of $\tan\beta$ and $\tan\gamma$, it nonetheless opens us the possibility of searching for the corresponding signals at the LHC, wherein one could attempt to isolate CP-violating asymmetries in the top-quark decay rates between the positively and negatively charged H_i^\pm ($i = 2, 3$) channels. The region of viable 3HDM parameter space in which these two states are both heavier than the top quark is much larger in comparison, and the mass difference $M_{H_2^\pm} - M_{H_3^\pm}$ can be up to 200 GeV or so, albeit for selected values of the other parameters so that the constraint from $\text{BR}(\bar{B} \rightarrow X_s \gamma)$ can be satisfied. In this case, while it may be difficult to access H_i^\pm signals in direct searches

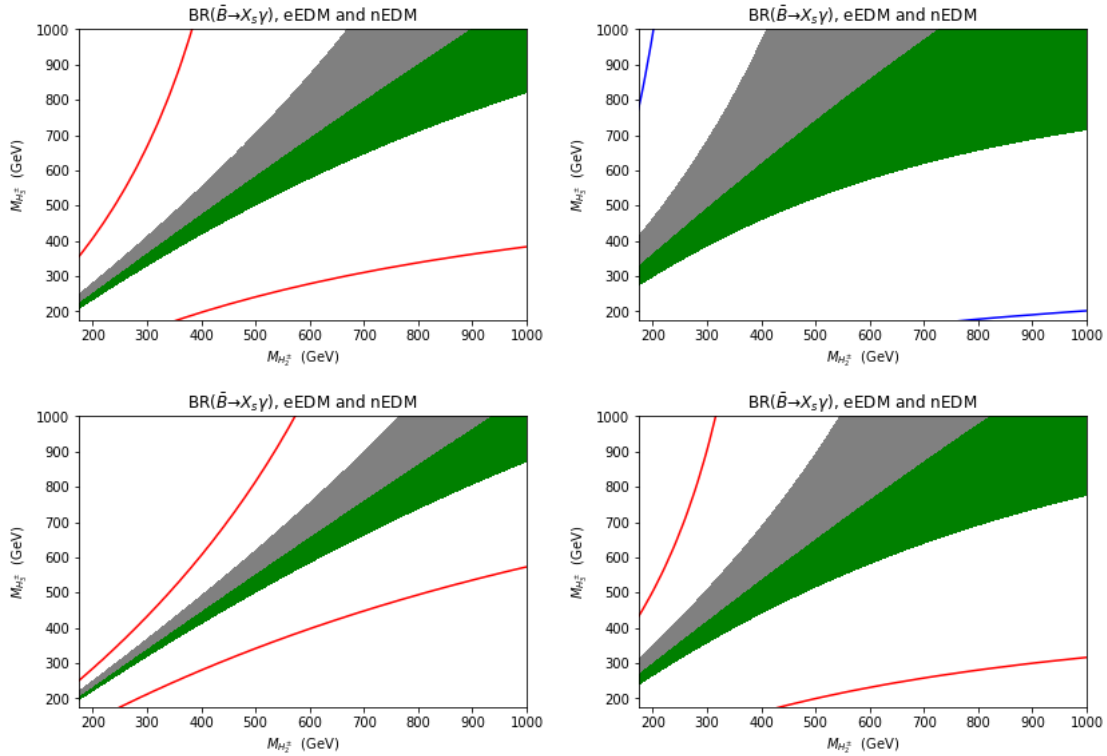


Figure 19. Same as Fig. 17 but with $\delta = 0.9\pi$.

at the LHC, and consequently the possible CP-violating nature of the 3HDM, the latter could well be established in CP asymmetries of $\bar{B} \rightarrow X_s/X_d\gamma$ observables at B -factories (e.g., Belle-II), as demonstrated in Ref. [36], which in fact can capture striking signals in the case of light charged Higgs bosons too.

Acknowledgments

This work was supported by the grant H2020-MSCA-RISE-2014 No. 645722 (NonMinimalHiggs). H.E.L. was also supported by the Natural Sciences and Engineering Research Council of Canada. S.M. is supported in part through the NExT Institute and the STFC Consolidated Grant No. ST/L000296/1. D.R.-C. is supported by the Royal Society Newton International Fellowship NIF/R1/180813 and by the National Science Centre (Poland) under the research Grant No. 2017/26/E/ST2/00470. D.R.-C. and M.S. thank Carleton University for hospitality during the initial stages of this work. The authors thank Shinya Kanemura and Kei Yagyu for useful conversations.

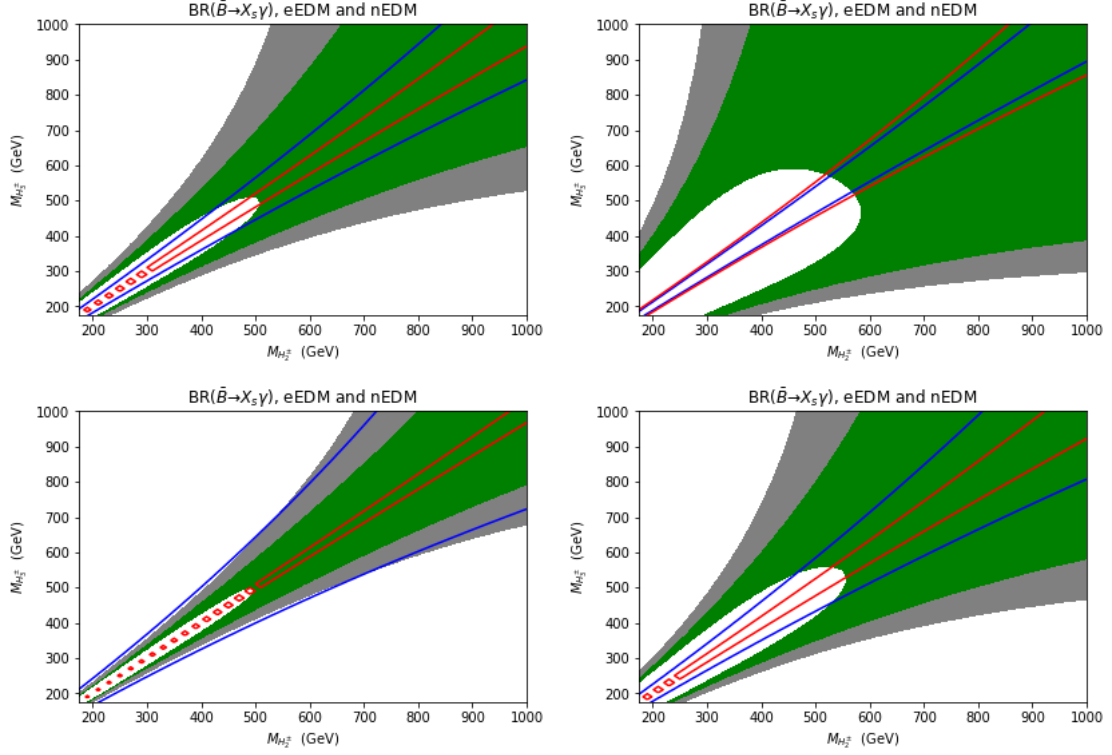


Figure 20. Same as Fig. 17 but with $\theta = -\pi/4$.

$m_c/m_b = 0.29$	$m_b - m_c = 3.39 \text{ GeV}$	$m_t = 173 \text{ GeV}$	$G_F = 1.1663787 \times 10^{-5} \text{ GeV}^{-2}$
$\alpha_{\text{em}} = 1/130.3$	$M_Z = 91.1875 \text{ GeV}$	$M_{W^\pm} = 80.33 \text{ GeV}$	$\alpha(M_Z) = 0.119$
$\lambda = 0.22650$	$A = 0.790$	$\bar{\rho} = 0.141$	$\bar{\eta} = 0.357$
$\text{BR}_{SL} = 0.1049$			

Table 3. Input values for the SM parameters. The central value of $\bar{B} \rightarrow X_s \gamma$ used here is obtained from these. We refer to [37] for the choice of fermion masses. The Wolfenstein parameters of the CKM matrix are taken from Ref. [28].

A Experimental constraints from $\bar{B} \rightarrow X_s \gamma$

Current values for the average experimental measurement [38] and SM prediction [39] for the $\text{BR}(\bar{B} \rightarrow X_s \gamma)$ are as follows:

$$\text{BR}(\bar{B} \rightarrow X_s \gamma)^{\text{exp}} = (3.32 \pm 0.15) \times 10^{-4} \text{ with } E_\gamma > 1.6 \text{ GeV}, \quad (\text{A.1})$$

$$\text{BR}(\bar{B} \rightarrow X_s \gamma)^{\text{SM}} = (3.40 \pm 0.17) \times 10^{-4} \text{ with } E_\gamma > 1.6 \text{ GeV}. \quad (\text{A.2})$$

In our $\text{BR}(\bar{B} \rightarrow X_s \gamma)$ numerical evaluation, we used the explicit formulas computed for the 2HDM with leading order (LO) and next-to-LO (NLO) effective Wilson coefficients running from the μ_W scale to μ_b with the scheme adopted in [37] and extrapolated it to 3HDM as in Ref. [36].

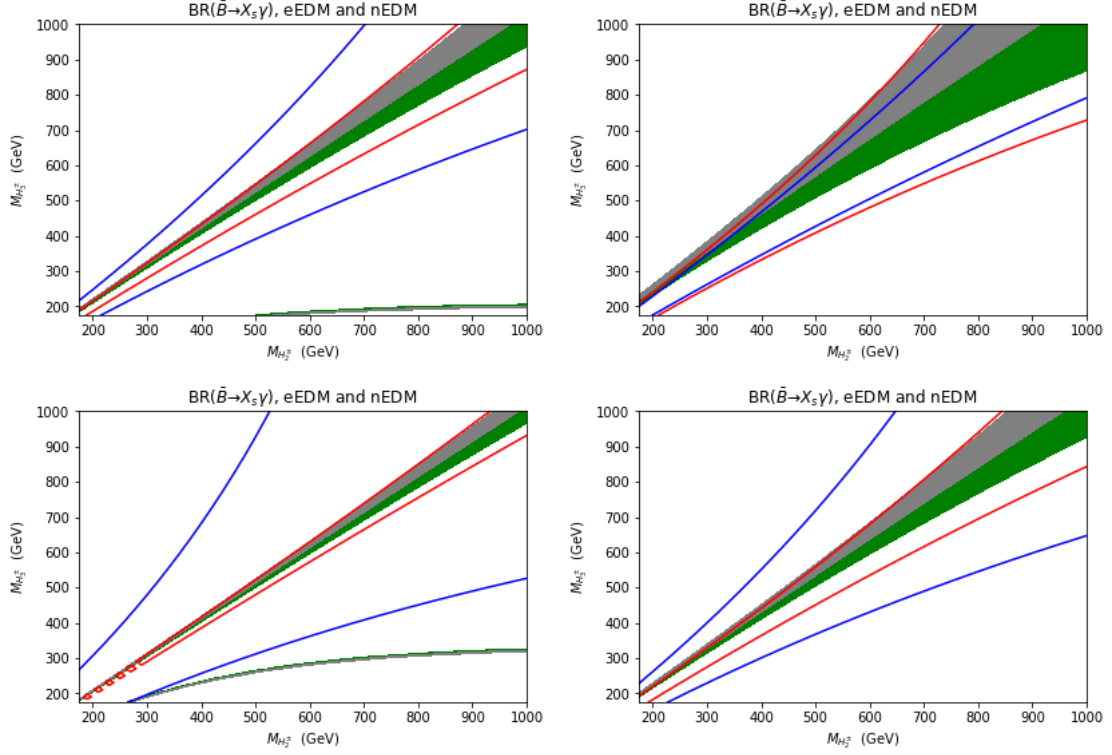


Figure 21. Same as Fig. 18 but with $\theta = -\pi/4$.

The two LO Wilson coefficients at the μ_W scale which are affected by charged Higgs contributions are $C_7^{0,\text{eff}}(\mu_W)$ and $C_8^{0,\text{eff}}(\mu_W)$, obtained as follows:

$$C_7^{0,\text{eff}}(\mu_W) = C_{7,SM}^0 + |Y_2|^2 C_{7,Y_2 Y_2}^0 + |Y_3|^2 C_{7,Y_3 Y_3}^0 + (X_2 Y_2^*) C_{7,X_2 Y_2}^0 + (X_3 Y_3^*) C_{7,X_3 Y_3}^0, \quad (\text{A.3})$$

$$C_8^{0,\text{eff}}(\mu_W) = C_{8,SM}^0 + |Y_2|^2 C_{8,Y_2 Y_2}^0 + |Y_3|^2 C_{8,Y_3 Y_3}^0 + (X_2 Y_2^*) C_{8,X_2 Y_2}^0 + (X_3 Y_3^*) C_{8,X_3 Y_3}^0, \quad (\text{A.4})$$

where $|Y_2|^2$, $|Y_3|^2$, $(X_2 Y_2^*)$, and $(X_3 Y_3^*)$ are the contribution of charged Higgs mixing couplings. The other LO Wilson coefficients are $C_2^{0,\text{eff}}(\mu_W) = 1$ and $C_i^{0,\text{eff}}(\mu_W) = 0$ ($i = 1, 3, 4, 5, 6$). The SM contributions are functions of m_t^2/M_W^2 while the charged Higgs contributions are functions of $m_t^2/M_{H_2^\pm}^2$ and $m_t^2/M_{H_3^\pm}^2$, entering the $C_{n,SM}^0$, $C_{n,X_2 Y_2}^0$, $C_{n,X_3 Y_3}^0$ ($n = 7, 8$) terms in Ref. [37].

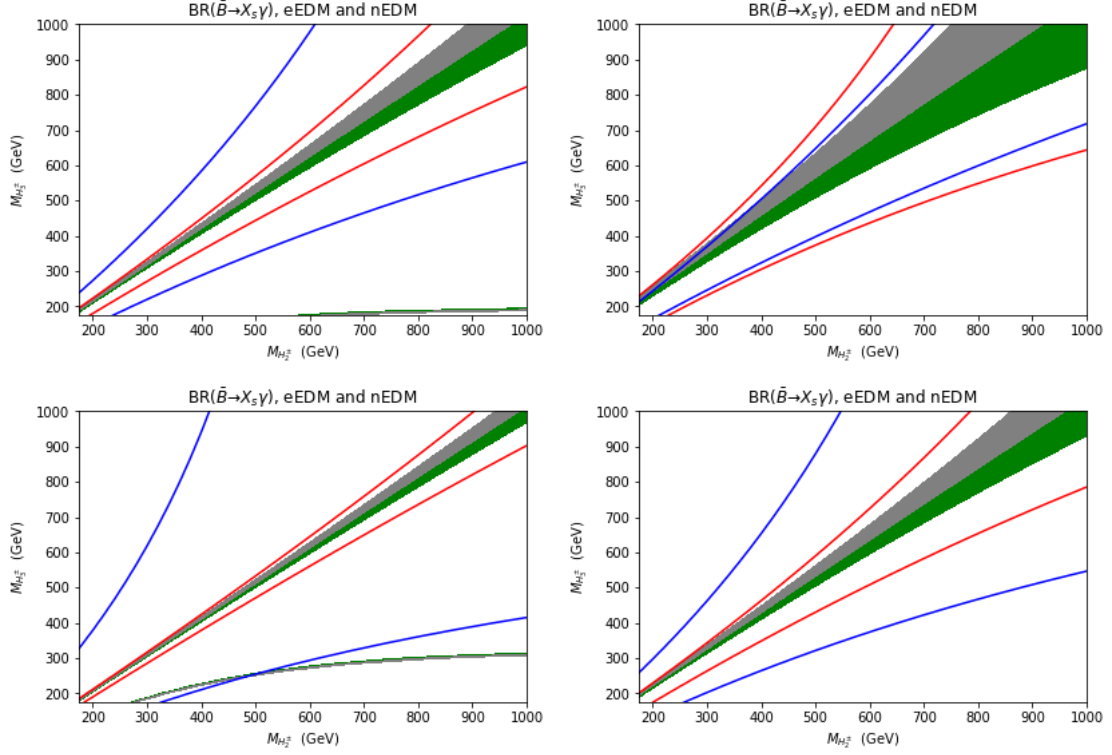


Figure 22. Same as Fig. 19 but with $\theta = -\pi/4$.

The NLO Wilson coefficients at the matching scale (μ_W) are as follow:

$$C_1^{1,\text{eff}}(\mu_W) = 15 + 6 \ln \frac{\mu_W^2}{M_W^2}, \quad (\text{A.5})$$

$$C_4^{1,\text{eff}}(\mu_W) = E_0 + \frac{2}{3} \ln \frac{\mu_W^2}{M_W^2} + |Y_2|^2 E_{H_2} + |Y_3|^2 E_{H_3}, \quad (\text{A.6})$$

$$C_i^{1,\text{eff}}(\mu_W) = 0 \quad (i = 2, 3, 5, 6), \quad (\text{A.7})$$

$$C_7^{1,\text{eff}}(\mu_W) = C_{7,SM}^{1,\text{eff}}(\mu_W) + |Y_2|^2 C_{7,Y_2 Y_2}^{1,\text{eff}}(\mu_W) + |Y_3|^2 C_{7,Y_3 Y_3}^{1,\text{eff}}(\mu_W) \\ + (X_2 Y_2^*) C_{7,X_2 Y_2}^{1,\text{eff}}(\mu_W) + (X_3 Y_3^*) C_{7,X_3 Y_3}^{1,\text{eff}}(\mu_W), \quad (\text{A.8})$$

$$C_8^{1,\text{eff}}(\mu_W) = C_{8,SM}^{1,\text{eff}}(\mu_W) + |Y_2|^2 C_{8,Y_2 Y_2}^{1,\text{eff}}(\mu_W) + |Y_3|^2 C_{8,Y_3 Y_3}^{1,\text{eff}}(\mu_W) \\ + (X_2 Y_2^*) C_{8,X_2 Y_2}^{1,\text{eff}}(\mu_W) + (X_3 Y_3^*) C_{8,X_3 Y_3}^{1,\text{eff}}(\mu_W). \quad (\text{A.9})$$

Explicit forms for all functions are given in [37]. Renormalization group running is then used to evaluate the Wilson coefficients at the scale $\mu = m_b$. The $\bar{B} \rightarrow X_s \gamma$ decay rates

can then be evaluated through

$$\Gamma(\bar{B} \rightarrow X_s \gamma) = \frac{G_F^2}{32\pi^4} |V_{ts}^* V_{tb}|^2 \alpha_{em} m_b^5 \times \left\{ |\bar{D}|^2 + A + \frac{\delta_\gamma^{NP}}{m_b^2} |C_7^{0,\text{eff}}(\mu_b)|^2 + \frac{\delta_c^{NP}}{m_c^2} \text{Re} \left[[C_7^{0,\text{eff}}(\mu_b)]^* \times \left(C_2^{0,\text{eff}}(\mu_b) - \frac{1}{6} C_1^{0,\text{eff}}(\mu_b) \right) \right] \right\}, \quad (\text{A.10})$$

$$\text{BR}(\bar{B} \rightarrow X_s \gamma) = \frac{\Gamma(\bar{B} \rightarrow X_s \gamma)}{\Gamma_{SL}} \text{BR}_{SL}. \quad (\text{A.11})$$

where the expressions for $|\bar{D}|$ ($b \rightarrow s\gamma$), A ($b \rightarrow s\gamma g$), and the semileptonic width Γ_{SL} are taken from [37]. For our $\text{BR}(\bar{B} \rightarrow X_s \gamma)$ numerical evaluations, we took the Tab. 3 input values as SM parameters. In such a case, m_c , m_b and m_t are pole masses of the charm-, bottom- and top-quark, respectively, and A , λ , $\bar{\rho}$ and $\bar{\eta}$ are the Wolfenstein parameters of the CKM matrix taken from Ref. [28].

Our implementation of the $\text{BR}(\bar{B} \rightarrow X_s \gamma)$ calculation yields a SM value of 3.39×10^{-4} , which is extremely close to the result of the state-of-the-art calculation given in Eq. (A.2). In the figures in this paper we use coloured bands to indicate the allowed range of $\pm 2\sigma$ about the experimental central value, where we have combined the experimental and theoretical uncertainties in quadrature. In particular, we show values of $\text{BR}(\bar{B} \rightarrow X_s \gamma)$ in the range $(3.32\text{--}3.77) \times 10^{-4}$ in grey and values in the range $(2.87\text{--}3.32) \times 10^{-4}$ in green.¹⁹

B Charged Higgs Yukawa couplings

In this section we collect the combinations of the Yukawa coupling coefficients X_i , Y_i , and Z_i ($i = 2, 3$) that appear in the various calculations in this paper, and give their expressions as a function of the four mixing parameters (θ , $\tan \gamma$, $\tan \beta$ and δ) in the Democratic 3HDM. We use the shorthand notation s_θ , c_θ , t_θ for $\sin \theta$, $\cos \theta$, and $\tan \theta$, respectively, and analogously for the other angles.

Starting from Eqs. (2.17) and (2.20), the Yukawa coupling coefficients in our parame-

¹⁹By coincidence, these ranges are equivalent to taking the 3σ allowed range using the experimental uncertainty only.

terization are:

$$X_2 = \frac{U_{12}^\dagger}{U_{11}^\dagger} = \frac{-c_\theta s_\beta(c_\delta + i s_\delta) - s_\theta c_\gamma c_\beta}{c_\beta s_\gamma}, \quad (\text{B.1})$$

$$Y_2 = -\frac{U_{22}^\dagger}{U_{21}^\dagger} = \frac{-c_\theta c_\beta(c_\delta + i s_\delta) + s_\theta c_\gamma s_\beta}{s_\beta s_\gamma}, \quad (\text{B.2})$$

$$Z_2 = \frac{U_{32}^\dagger}{U_{31}^\dagger} = \frac{s_\theta s_\gamma}{c_\gamma}, \quad (\text{B.3})$$

$$X_3 = \frac{U_{13}^\dagger}{U_{11}^\dagger} = \frac{s_\theta s_\beta(c_\delta + i s_\delta) - c_\theta c_\gamma c_\beta}{c_\beta s_\gamma}, \quad (\text{B.4})$$

$$Y_3 = -\frac{U_{23}^\dagger}{U_{21}^\dagger} = \frac{s_\theta c_\beta(c_\delta + i s_\delta) + c_\theta c_\gamma s_\beta}{s_\beta s_\gamma}, \quad (\text{B.5})$$

$$Z_3 = \frac{U_{33}^\dagger}{U_{31}^\dagger} = \frac{c_\theta s_\gamma}{c_\gamma}. \quad (\text{B.6})$$

The combinations that appear in the EDM calculations are:

$$\text{Im}(-X_2 Y_2^*) = \frac{s_\theta c_\theta s_\delta}{s_\beta c_\beta s_\gamma t_\gamma} = -\text{Im}(-X_3 Y_3^*), \quad (\text{B.7})$$

$$\text{Im}(-Y_2^* Z_2) = -\frac{s_\theta c_\theta s_\delta}{t_\beta c_\gamma} = -\text{Im}(-Y_3^* Z_3). \quad (\text{B.8})$$

The following contribute to the calculation of $\text{BR}(\bar{B} \rightarrow X_s \gamma)$. The real components of $X_i Y_i^*$ ($i = 2, 3$) are as follows:

$$\text{Re}(X_2 Y_2^*) = \frac{c_\theta^2}{s_\gamma^2} + \frac{c_\delta c_\theta s_\theta}{t_\beta t_\gamma s_\gamma} - \frac{c_\delta t_\beta c_\theta s_\theta}{t_\gamma s_\gamma} - \frac{s_\theta^2}{t_\gamma^2}, \quad (\text{B.9})$$

$$\text{Re}(X_3 Y_3^*) = \frac{s_\theta^2}{s_\gamma^2} + \frac{c_\delta t_\beta c_\theta s_\theta}{t_\gamma s_\gamma} - \frac{c_\delta c_\theta s_\theta}{t_\beta t_\gamma s_\gamma} - \frac{c_\theta^2}{t_\gamma^2}. \quad (\text{B.10})$$

Finally for $|Y_2^2|$ and $|Y_3^2|$ we have:

$$|Y_2^2| = \frac{c_\delta^2 c_\theta^2}{t_\beta^2 s_\gamma^2} - \frac{s_\delta^2 c_\theta^2}{t_\beta^2 s_\gamma^2} - \frac{2c_\delta c_\theta s_\theta}{t_\beta t_\gamma s_\gamma} + \frac{s_\theta^2}{t_\gamma^2}, \quad (\text{B.11})$$

$$|Y_3^2| = \frac{c_\delta^2 s_\theta^2}{t_\beta^2 s_\gamma^2} - \frac{s_\delta^2 s_\theta^2}{t_\beta^2 s_\gamma^2} + \frac{2c_\delta c_\theta s_\theta}{t_\beta t_\gamma s_\gamma} + \frac{c_\theta^2}{t_\gamma^2}. \quad (\text{B.12})$$

References

- [1] L. Canetti, M. Drewes and M. Shaposhnikov, *Matter and antimatter in the universe*, *New J. Phys.* **14** (2012) 095012 [[1204.4186](#)].
- [2] A. Sakharov, *Violation of CP Invariance, C asymmetry, and baryon asymmetry of the universe*, *Sov. Phys. Usp.* **34** (1991) 392.
- [3] nEDM collaboration, *Measurement of the permanent electric dipole moment of the neutron, EDM*, *Phys. Rev. Lett.* **124** (2020) 081803 [[2001.11966](#)].

- [4] ACME collaboration, *Improved limit on the electric dipole moment of the electron, edm*, *Nature* **562** (2018) 355.
- [5] A. Cordero-Cid, J. Hernández-Sánchez, V. Keus, S.F. King, S. Moretti, D. Rojas et al., *CP violating scalar Dark Matter*, *Journal of High Energy Physics* **2016** (2016) 014 [[1608.01673](#)].
- [6] D. Azevedo, P.M. Ferreira, M.M. Muhlleitner, S. Patel, R. Santos and J. Wittbrodt, *CP in the dark*, *JHEP* **11** (2018) 091 [[1807.10322](#)].
- [7] M. Carena, M. Quirós and Y. Zhang, *Electroweak Baryogenesis from Dark-Sector CP Violation*, *Phys. Rev. Lett.* **122** (2019) 201802 [[1811.09719](#)].
- [8] S. Okawa, M. Pospelov and A. Ritz, *Electric Dipole Moments From Dark Sectors, EDM*, *Phys. Rev. D* **100** (2019) 075017 [[1905.05219](#)].
- [9] M. Carena, M. Quirós and Y. Zhang, *Dark CP violation and gauged lepton or baryon number for electroweak baryogenesis*, *Phys. Rev. D* **101** (2020) 055014 [[1908.04818](#)].
- [10] V. Keus, *Dark origins of matter-antimatter asymmetry*, *PoS CORFU2019* (2020) 059 [[2003.02141](#)].
- [11] A. Cordero-Cid, J. Hernández-Sánchez, V. Keus, S. Moretti, D. Rojas-Ciofalo and D. Sokołowska, *Collider signatures of dark CP violation*, *Physical Review D* **101** (2020) 095023 [[2002.04616](#)].
- [12] S. Kanemura, M. Kubota and K. Yagyu, *Aligned CP-violating Higgs sector canceling the electric dipole moment, EDM*, *JHEP* **08** (2020) 026 [[2004.03943](#)].
- [13] S. Glashow, J. Iliopoulos and L. Maiani, *Weak interactions with lepton-hadron symmetry*, *Phys. Rev. D* **2** (1970) 1285.
- [14] S.L. Glashow and S. Weinberg, *Natural conservation laws for neutral currents*, *Phys. Rev. D* **15** (1977) 1958.
- [15] E.A. Paschos, *Diagonal neutral currents*, *Physical Review D* **15** (1977) 1966.
- [16] M. Jung and A. Pich, *Electric Dipole Moments in Two-Higgs-Doublet Models, EDM*, *JHEP* **04** (2014) 076 [[1308.6283](#)].
- [17] G. Cree and H.E. Logan, *Yukawa alignment from natural flavor conservation*, *Phys. Rev. D* **84** (2011) 055021 [[1106.4039](#)].
- [18] A. Akeroyd, S. Moretti, K. Yagyu and E. Yildirim, *Light charged Higgs boson scenario in 3-Higgs doublet models*, *Int. J. Mod. Phys. A* **32** (2017) 1750145 [[1605.05881](#)].
- [19] Y. Grossman, *Phenomenology of models with more than two Higgs doublets*, *Nucl. Phys. B* **426** (1994) 355 [[hep-ph/9401311](#)].
- [20] A. Belyaev, N.D. Christensen and A. Pukhov, *CalcHEP 3.4 for collider physics within and beyond the Standard Model*, *Computer Physics Communications* **184** (2013) 1729 [[1207.6082](#)].
- [21] M. Guchait and S. Moretti, *Improving the discovery potential of charged Higgs bosons at Tevatron run II*, *JHEP* **01** (2002) 001 [[hep-ph/0110020](#)].
- [22] K. Assamagan, M. Guchait and S. Moretti, *Charged Higgs bosons in the transition region $M(H^\pm) \sim m(t)$ at the LHC*, in *3rd Les Houches Workshop on Physics at TeV Colliders*, 2, 2004 [[hep-ph/0402057](#)].

- [23] A. Akeroyd, S. Moretti and M. Song, *Light charged Higgs boson with dominant decay to quarks and its search at the LHC and future colliders*, *Phys. Rev. D* **98** (2018) 115024 [[1810.05403](#)].
- [24] A. Akeroyd, S. Moretti and M. Song, *Light charged Higgs boson with dominant decay to a charm quark and a bottom quark and its search at LEP2 and future e^+e^- colliders*, *Phys. Rev. D* **101** (2020) 035021 [[1908.00826](#)].
- [25] CMS collaboration, *Search for charged Higgs bosons in the $H^\pm \rightarrow \tau^\pm \nu_\tau$ decay channel in proton-proton collisions at $\sqrt{s} = 13$ TeV*, *JHEP* **07** (2019) 142 [[1903.04560](#)].
- [26] CMS collaboration, *Search for a charged Higgs boson decaying to charm and bottom quarks in proton-proton collisions at $\sqrt{s} = 8$ TeV*, *JHEP* **11** (2018) 115 [[1808.06575](#)].
- [27] ATLAS collaboration, *Search for a light charged Higgs boson in the decay channel $H^\pm \rightarrow c\bar{s}$ in $t\bar{t}$ events using pp collisions at $\sqrt{s} = 7$ TeV with the ATLAS detector*, *Eur. Phys. J. C* **73** (2013) 2465 [[1302.3694](#)].
- [28] PARTICLE DATA GROUP collaboration, *Review of particle physics*, *PTEP* **2020** (2020) 083C01.
- [29] ATLAS collaboration, *Direct top-quark decay width measurement at $\sqrt{s} = 13$ TeV with the ATLAS experiment*, *PoS LeptonPhoton2019* (2019) 089.
- [30] V.D. Barger, J. Hewett and R. Phillips, *New Constraints on the Charged Higgs Sector in Two Higgs Doublet Models*, *Phys. Rev. D* **41** (1990) 3421.
- [31] D. Bowser-Chao, D. Chang and W.-Y. Keung, *Electron electric dipole moment from CP violation in the charged Higgs sector, EDM*, *Phys. Rev. Lett.* **79** (1997) 1988 [[hep-ph/9703435](#)].
- [32] M. Pospelov and I. Khriplovich, *Electric dipole moment of the W boson and the electron in the Kobayashi-Maskawa model, EDM*, *Sov. J. Nucl. Phys.* **53** (1991) 638.
- [33] D. Chang, W.-Y. Keung and T. Yuan, *Two loop bosonic contribution to the electron electric dipole moment, EDM*, *Phys. Rev. D* **43** (1991) 14.
- [34] B. Graner, Y. Chen, E.G. Lindahl and B.R. Heckel, *Reduced Limit on the Permanent Electric Dipole Moment of Hg199*, *Phys. Rev. Lett.* **116** (2016) 161601 [[1601.04339](#)].
- [35] E. Braaten, C.-S. Li and T.-C. Yuan, *The Evolution of Weinberg's Gluonic CP Violation Operator*, *Phys. Rev. Lett.* **64** (1990) 1709.
- [36] A. Akeroyd, S. Moretti, T. Shindou and M. Song, *CP asymmetries of $\bar{B} \rightarrow X_s/X_d \gamma$ in models with three Higgs doublets*, [2009.05779](#).
- [37] F. Borzumati and C. Greub, *2HDMs predictions for $\bar{B} \rightarrow X_s \gamma$ in NLO QCD*, *Phys. Rev. D* **58** (1998) 074004 [[hep-ph/9802391](#)].
- [38] HFLAV collaboration, *Averages of b-hadron, c-hadron, and τ -lepton properties as of 2018*, [1909.12524](#).
- [39] M. Misiak, A. Rehman and M. Steinhauser, *Towards $\bar{B} \rightarrow X_s \gamma$ at the NNLO in QCD without interpolation in m_c* , [2002.01548v2](#).